

博士論文

Electric field effects on excitons in individual carbon nanotubes
(単一カーボンナノチューブにおける励起子の電界効果に関する研究)

吉田 匡廣

THE UNIVERSITY OF TOKYO

**Electric field effects on excitons in
individual carbon nanotubes**

A thesis submitted in partial satisfaction
of the requirements for the degree of

Doctor of Philosophy

in

Engineering

by

Masahiro Yoshida

37-127096

Thesis Advisor
Professor Seigo Tarucha

August 2016

Electric field effects on excitons in individual carbon nanotubes

Copyright © 2016

by

Masahiro Yoshida

Acknowledgments

First, I thank Prof. Kato for supervising my experiments, teaching me how to do scientific writing, arranging a collaboration work with Ohio state university, and so on. Although obtaining a Ph.D. degree is really hard and challenging, I believe that my choice of going on to Ph.D. programs in Kato group was correct.

I also appreciate all of the students in Kato group. Great thanks to A. Ishii for giving me fantastic programs, helpful discussion, serving nice meals, and providing interesting topics on baseball and politics. Y. Kumamoto took excellent data on Stark effect in nanotubes, and his contribution in that project is high A. Popert measured so many nanotubes which showed trion emission, and wrote cool programs autonomously for our project. A. Yokoyama demonstrated giant circular dichroism in nanotubes, and gave me a chance that my name was put on an authors' list in his paper. T. Uda gave me nice information on device fabrication, and helped managing the group with me as a Ph.D. candidate. M. Jiang and N. Higashide optimized device fabrication process, especially electron-beam evaporators, which was useful for my experiments. S. Imamura, R. Miura, and X. Liu showed me great data and experimental skills, which are inspiring me. K. Fujisawa, and S. Lee brought our group their knowledge on transition metal dichalcogenide and device fabrication, respectively. H. Machiya, I. Kimura, and A. Sasabe are livening up Kato group right now, and I hope that they will get amazing results in their experiments. Y. Kawaguchi, T. Onoue, and K. Takahashi made their effort as undergraduate students, and presented interesting data. Y. Ueda observed trion in suspended nanotubes with me for the first time. Many foreign students provided opportunities of English communication to me, so I thank Emil Rofers, Jason Jung, Kornel Ozvoldik, Susanne Mosler, Simon Stuij, Michael Taylor, Bing Zhang, Alexander Unterkreuter, Ajay Subramanian, and Sunny Feng.

I'm grateful to Nakamura-san, Hirosawa-san, Sawamura-san, Dr. Kubota, Prof. Mita, and technical assistants in Takeda clean room for managing a lot of instruments such as an electron-beam lithography system. I thank Prof. Matsuda (Kyoto Univ.) for helpful discussions, Dr. Kan, Dr. Isozaki, and Prof. Shimoyama for the use of an electron beam evaporator, and O. Ohguchi and Prof. Yamamoto for the plasma etcher, and Dr. Inoue, Prof. Chiashi and Prof. Maruyama for a vacuum evaporator as well as an electron microscope. I thank Prof. Tarucha for helpful discussion and acceptance that I belong to his group this year. I appreciate Prof. Hasegawa (Dept. of chemistry) for advising me a lot

as a mentor for ALPS. I had many precious experiences at Ohio state university, and thank Prof. Johnston-Halperin, Prof. Myers, Dr. Pu, Dr. Yu, Yu-Sheng Ou, and other group members.

I thank ALPS for supporting me, and the Sasakawa Scientific Research Grant helped my project on trions in carbon nanotubes.

Finally, I would like to appreciate my parents for supporting me.

Abstract

Electric field effects on excitons in individual carbon nanotubes

by

Masahiro Yoshida

Single-walled carbon nanotubes are emitters at telecom wavelengths which can be directly grown on silicon, being promising materials for nanoscale optoelectronic devices. Due to limited screening of Coulomb interaction in nanotubes, excitons play a key role in light emission, and therefore understanding the excitonic properties under electric fields is important. Here, we have investigated the electric field effects on excitons in individual suspended nanotubes within field effect transistor structures, and elucidated various phenomena such as spontaneous exciton dissociation, Stark effect, and trion (charged exciton) emission.

Simultaneous photoluminescence and photocurrent measurements on individual single-walled carbon nanotubes have revealed spontaneous dissociation of excitons into free electron-hole pairs. Correlation of luminescence intensity and photocurrent shows that a significant fraction of excitons are dissociating before recombination. The combination of optical and electrical signals also allows for extraction of the absorption cross section and the oscillator strength. Our observations explain the reasons for photoconductivity measurements in single-walled carbon nanotubes being straightforward despite the large exciton binding energies.

We have also investigated electric-field induced redshifts of photoluminescence from individual nanotubes. The shifts scale quadratically with field, while measurements with different excitation powers and energies show that effects from heating and relaxation pathways are small. We attribute the shifts to the Stark effect, and characterize nanotubes with different chiralities. By taking into account exciton binding energies for air-suspended tubes, we find that theoretical predictions are in quantitative agreement.

Finally, we report on the observation of trion emission from suspended carbon nanotubes where carriers are introduced electrostatically by gate voltages. The trion peak emerges below the E_{11} emission energy at gate voltages that coincide

with the onset of bright exciton quenching. By investigating nanotubes with various chiralities, we verify that the energy separation between the bright exciton peak and the trion peak becomes smaller for larger diameter tubes. Trion binding energies that are significantly larger compared to surfactant-wrapped carbon nanotubes are obtained, and the difference is attributed to the reduced dielectric screening in suspended tubes.

These results demonstrate electrical control of excitons in carbon nanotubes. Measurements on individual chirality-assigned nanotubes allow for elimination of inhomogeneous broadening and chirality dependent band structure modulation, which complicate ensemble measurements. In order to investigate chirality dependence, an automated optical setup has been constructed for efficient data collection. Through quantitative discussion on electric field effects on excitons in individual nanotubes, this work provides important insights to exciton physics in carbon nanotubes for applications in nanoscale optoelectronic devices.

Contents

Acknowledgments	iii
Abstract	v
Abbreviations	xiii
Chapter 1 Introduction	1
1.1 Single-walled carbon nanotubes	1
1.1.1 Structure	1
1.1.2 Electronic structure	4
1.1.3 Optical properties	7
1.1.4 Excitons and charged excitons in nanotubes	9
1.2 Carbon nanotube optoelectronics	13
1.2.1 Advantages and unique characteristics	13
1.2.2 Previous works on electric field effects on excitons in nanotubes	13
1.2.3 Issues and difficulties	16
1.3 Research objective	17
1.4 Organization	18
Chapter 2 Carbon nanotube field effect transistors	19
2.1 Sample description	19
2.2 Device fabrication	21
Chapter 3 Bias voltage effects on excitons in individual suspended carbon nanotubes	27
3.1 Simultaneous photoluminescence and photocurrent measurements	27
3.1.1 Background on bias voltage effects on excitons in nanotubes	27
3.1.2 Optical setup	28
3.1.3 Imaging	29

3.1.4	Excitation spectroscopy	30
3.2	Spontaneous exciton dissociation in carbon nanotubes	31
3.2.1	Exciton dissociation in nanotubes	31
3.2.2	Excitation power and bias voltage dependences	32
3.2.3	Absorption cross section and oscillator strength	36
3.3	Stark effect of excitons in individual air-suspended carbon nanotubes	37
3.3.1	Stark effect in nanotubes	37
3.3.2	Electric field dependences of photoluminescence and current	38
3.3.3	Redshifts induced by Stark effect and heating	40
3.3.4	Chirality dependence	43
3.4	Conclusions	44
 Chapter 4 Gate-voltage induced trions in suspended carbon nanotubes		47
4.1	Trions in nanotubes	47
4.2	Photoluminescence measurement system	48
4.3	Photoluminescence line scan measurements	51
4.4	Photoluminescence excitation spectroscopy with and without gate voltages	51
4.5	Gate voltage dependence of photoluminescence	53
4.6	Nanotube diameter dependence	55
4.6.1	Individual nanotubes	55
4.6.2	Bundled nanotubes	57
4.7	Conclusions and outlook	57
 Chapter 5 Conclusions		59
 Appendix A Raman spectroscopy		61
 Appendix B Heat conduction equation		63
 References		65
 List of publications and presentations		77

List of Figures

1.1	Graphene lattice when the (6,4) carbon nanotube is opened (light blue area)	2
1.2	Brillouin zone of a (6,4) SWCNT (purple lines) mapped onto graphene Brillouin zone.	4
1.3	Band structure of graphene.	6
1.4	Brillouin zones of (4,0), (5,0), and (6,0) nanotubes (black and green lines).	7
1.5	Density of states for a semiconducting SWCNT	8
1.6	Schematics of polarized light (E_{ext}) parallel (a) and perpendicular (b) to tube axis. E_{in} indicates depolarization fields.	8
1.7	Excitons in carbon nanotubes.	9
1.8	Band diagram of SWCNTs.	10
1.9	Energy diagram of E_{11} excitons in SWCNTs (about 1 nm diameter).	10
1.10	Excitons and trions (or charged excitons) in a carbon nanotube	12
1.11	Illustration of renormalization of band-gap and exciton binding energies in a doped carbon nanotube.	16
1.12	Photoluminescence excitation spectroscopy.	18
2.1	Schematics of devices	19
2.2	Sample layout	20
2.3	Device fabrication processes	22
2.4	Optical microscope images of devices	26
2.5	Scanning electron micrographs of devices	26
3.1	Simultaneous photoluminescence and photocurrent measurements.	28
3.2	A schematic of an optical setup.	29
3.3	Simultaneous photoluminescence and photocurrent images.	30
3.4	Simultaneous photoluminescence and photocurrent excitation spectra.	31

3.5	Excitation power and bias voltage dependences.	33
3.6	Bias voltage dependence of PL under E_{12} resonant excitation. . .	34
3.7	PL spectra taken with electric fields.	39
3.8	Electric field dependence of emission energy, full width at half maximum, peak area on photoluminescence. Current and dark current as a function of electric field.	40
3.9	Excitation power dependence of current, broadening, and redshift. Field-induced redshift as a function of electric field taken at different excitation energies.	42
3.10	Redshift as a function of broadening for different electric fields. . .	42
3.11	Stark effect for different chirality nanotubes. Diameter dependence of Stark effect.	43
4.1	Schematic of photoluminescence measurement system.	50
4.2	Photoluminescence measurement system in optics lab	50
4.3	A PLE map of an individual nanotube. Photoluminescence spectra with and without gate voltages. Photoluminescence excitation maps with and without gate voltages.	52
4.4	PL spectra as a function of gate voltage. Gate voltage dependence of peak area and blueshift	54
4.5	PL spectra for (8,6), (9,7), and (14,3) nanotubes. Nanotube diameter dependence of energy separation between E_{11} and the trion peaks.	56
4.6	PLE maps and PL spectra for individual and bundled (8,6) nanotubes.	58
A.1	Raman spectra	62
B.1	Heat conduction equation.	63

List of Tables

1.1	Classification and structural parameters of single-walled carbon nanotubes.	3
2.1	Description of wafer and device parameters.	20
2.2	Summary of fabrication process (trench formation and annealing).	23
2.3	Summary of fabrication process (metal deposition).	24
2.4	Summary of fabrication process (growth of carbon nanotubes).	25
3.1	Absorption cross section and oscillator strength for the eight nanotubes measured.	37
4.1	Specifications of OMA-V 1.7 and 2.2	49

Abbreviations

AB	Aharonov Bohm
BS	beam splitter
CVD	chemical vapor deposition
CW	continuous wave
DOS	density of states
EBL	electron-beam lithography
E/O	electrical-to-optical
FET	field-effect transistor
FWHM	full-width at half maximum
HWP	half-wave plate
ICP	inductively coupled plasma
IR	infrared
NA	numerical aperture
ND	neutral density
NIR	near-infrared
PC	photocurrent
PL	photoluminescence
PLE	photoluminescence excitation
RBM	radial breathing mode
RT	room temperature
SEM	scanning electron microscopy
SWCNT	single-walled carbon nanotube
TMAH	tetramethyl ammonium hydroxide

Chapter 1

Introduction

In this chapter, we give an introduction on physical properties of single-walled carbon nanotubes (SWCNTs) [1] and describe how nanotubes are promising for fundamental studies of nanocarbon materials as well as future applications in optoelectronic devices. Next, we review previous studies on optical properties of nanotubes under electric field, and point out some issues on investigating those properties. Finally, we present our research objectives and show methods for addressing the issues.

1.1 Single-walled carbon nanotubes

1.1.1 Structure

Single-walled carbon nanotubes in real space

A SWCNT is a nanoscale hollow cylinder that is made by rolling up a single graphite layer, which is called graphene.¹ Figure 1.1 shows a graphene honeycomb lattice when a SWCNT is opened up. The line AB corresponds to the circumference of the SWCNT, and the vector \vec{AB} is called the chiral vector, \mathbf{C}_h .

¹There are mainly two types of CNTs. One is the SWCNT and the other is multi-walled carbon nanotube which is composed of a number of graphene layers. In this thesis, only SWCNTs are explained.

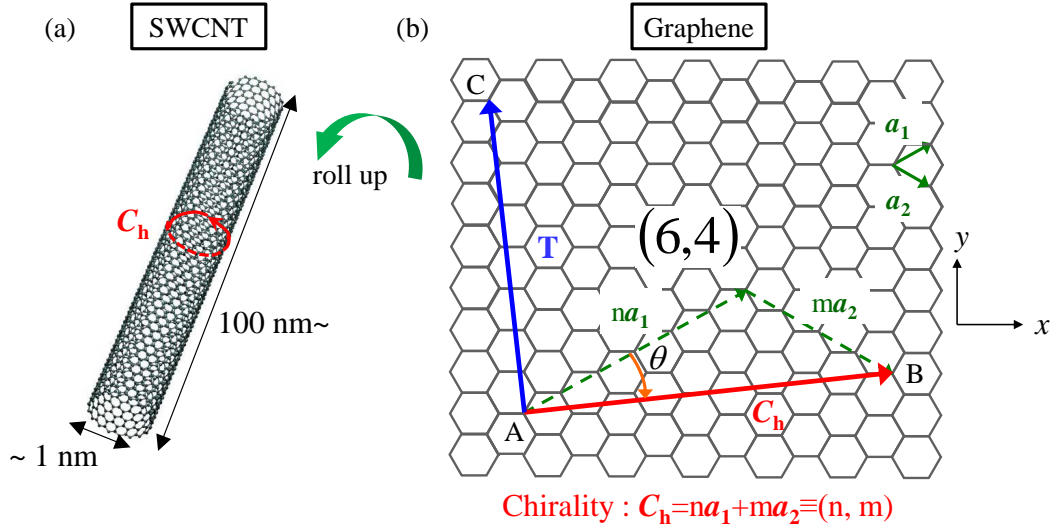


Figure 1.1: (a) A single-walled carbon nanotube. (b) Graphene lattice when the (6, 4) tube is opened (light blue area). Red, blue, green and orange lines represent chiral vector, transverse vector, lattice vectors, and chiral angles, respectively.

When lattice vectors are given by \mathbf{a}_1 and \mathbf{a}_2 , \mathbf{C}_h is

$$\mathbf{C}_h = n\mathbf{a}_1 + m\mathbf{a}_2 \equiv (n, m), \quad (1.1)$$

$$\mathbf{a}_1 = \frac{\sqrt{3}}{2}a\mathbf{x} + \frac{1}{2}a\mathbf{y}, \quad \mathbf{a}_2 = \frac{\sqrt{3}}{2}a\mathbf{x} - \frac{1}{2}a\mathbf{y}, \quad (1.2)$$

where n and m are integers and satisfy $0 \leq m \leq n$. The pair of the integers, (n, m) , is called chirality. For example, chirality is (6, 4) in Fig. 1.1. Interestingly, electronic structure of SWCNTs depends on chirality as discussed in Sec.1.1.2.

In order to describe the electronic structure of SWCNTs, some parameters will be defined below. The circumference length $L = |\mathbf{C}_h|$, the diameter d_t , the chiral angle θ of SWCNTs are

$$L \equiv |\mathbf{C}_h| = a\sqrt{n^2 + m^2 + nm}, \quad (1.3)$$

$$d_t \equiv \frac{L}{\pi} = \frac{a\sqrt{n^2 + m^2 + nm}}{\pi}, \quad (1.4)$$

$$\theta = \arctan \frac{\sqrt{3}m}{2n + m}, \quad (1.5)$$

where $a = |\mathbf{a}_1| = |\mathbf{a}_2| = 2.49 \text{ \AA}$ is the lattice constant of the honeycomb lattice.²

²The length between nearest-neighbor carbon atoms in SWCNTs, a_{C-C} , is 1.44 \AA , so $a = \sqrt{3}a_{C-C}$ is satisfied.

Table 1.1: Classification and structural parameters of single-walled carbon nanotubes.

Name	\mathbf{C}_h	d_t	\mathbf{T}	θ
armchair	(n, n)	$\sqrt{3}na/\pi$	$(1, -1)$	30°
zig-zag	$(n, 0)$	na/π	$(1, -2)$	0°
chiral	(n, m)	$a\sqrt{n^2 + m^2 + nm}/\pi$	$(\frac{2m+n}{d_R}, -\frac{2n+m}{d_R})$	$\arctan \frac{\sqrt{3}m}{2n+m}$
chiral	$(6, 4)$	$a\sqrt{76}/\pi = 0.69 \text{ nm}$	$(7, -8)$	$\arctan \frac{\sqrt{3}}{4} = 23.4^\circ$

In Fig. 1.1, point C is defined as the first lattice point that is encountered when drawing a line transverse to \mathbf{C}_h from point A. \vec{AC} is called the transverse vector \mathbf{T} , which is parallel to the axial direction of the SWCNT. \mathbf{T} is given by

$$\mathbf{T} = t_1 \mathbf{a}_1 + t_2 \mathbf{a}_2 \equiv (t_1, t_2), \quad (1.6)$$

$$t_1 = \frac{2m+n}{d_R}, t_2 = -\frac{2n+m}{d_R}, \quad (1.7)$$

where the highest common factor (HCF) between t_1 and t_2 is 1, and d_R is HCF between $(2m+n)$ and $(2n+m)$. In the case of Fig. 1.1, (t_1, t_2) is $(7, -8)$.

It is known that SWCNTs are classified into three types by symmetry. SWCNTs with chirality of (n, n) and $(n, 0)$ are called armchair and zig-zag nanotubes, respectively, due to their cross-sectional configuration of carbon atoms.³ Armchair and zig-zag nanotubes are achiral. On the other hand, $(n, m) : 0 < m < n$ nanotubes are called chiral nanotubes because of the helical symmetry which armchair and zig-zag nanotubes do not have. In Table.1.1, the parameters defined above are summarized for the three types of SWCNTs.

Single-walled carbon nanotubes in reciprocal space

To understand the band structure of SWCNTs, it is necessary to introduce the reciprocal space of graphene.

From Eq.(1.2), reciprocal lattice vectors \mathbf{b}_1 and \mathbf{b}_2 can be defined,

$$\mathbf{b}_1 = \frac{2\pi}{a} \left(\frac{1}{\sqrt{3}} \mathbf{k}_x + \mathbf{k}_y \right), \quad \mathbf{b}_2 = \frac{2\pi}{a} \left(\frac{1}{\sqrt{3}} \mathbf{k}_x - \mathbf{k}_y \right). \quad (1.8)$$

³From the chemical point of view, the difference between armchair and zig-zag nanotubes is that the cross-sectional configurations of former and latter are cis and trans type.

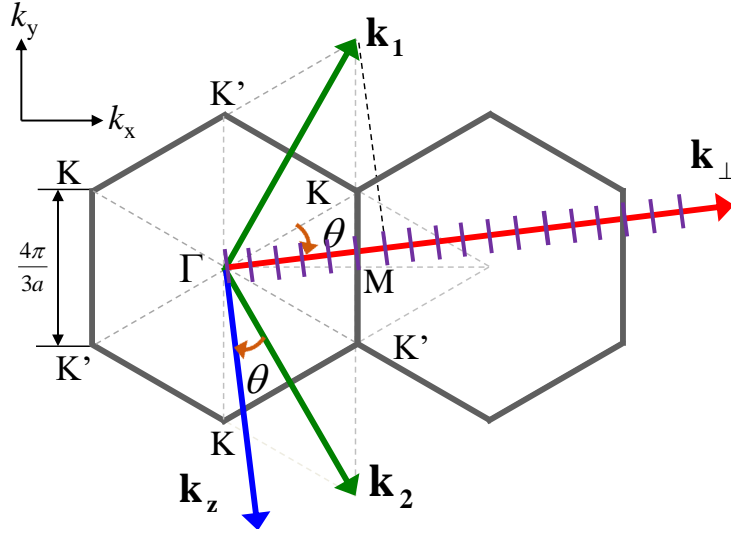


Figure 1.2: Brillouin zone of a (6,4) SWCNT (purple lines) mapped onto graphene Brillouin zone.

In addition, wave vectors \mathbf{k}_\perp and \mathbf{k}_z are defined under the following conditions,

$$\mathbf{C}_h \cdot \mathbf{k}_\perp = 2\pi, \quad \mathbf{C}_h \cdot \mathbf{k}_z = 0, \quad \mathbf{T} \cdot \mathbf{k}_\perp = 0, \quad \mathbf{T} \cdot \mathbf{k}_z = 2\pi, \quad (1.9)$$

which mean that \mathbf{k}_\perp and \mathbf{k}_z in reciprocal space correspond to \mathbf{C}_h and \mathbf{T} in real space. From these equations,

$$\mathbf{k}_\perp = \frac{1}{N}(-t_2\mathbf{b}_1 + t_1\mathbf{b}_2), \quad \mathbf{k}_z = \frac{1}{N}(m\mathbf{b}_1 - n\mathbf{b}_2), \quad (1.10)$$

$$|\mathbf{k}_\perp| = \frac{2}{d_t}, \quad |\mathbf{k}_z| = \frac{2\pi}{|\mathbf{T}|}, \quad (1.11)$$

where $N = n^2 + nm + m^2$. Figure 1.2 shows the Brillouin zone for (6, 4) SWCNT's case, and the purple lines are called cutting lines. Detailed explanation will be given in Sec.1.1.2.

1.1.2 Electronic structure

Band structure of graphene by tight-binding calculation

Usually a carbon atom's electron orbital state is $(1s)^2(2s)^2(2p)^2$. Because of the two dimensionality of graphene, however, sp^2 orbital hybridization occurs and therefore graphene orbital becomes $(1s)^2(2s)^1(2p)^3$. It is known that π bonds of graphene, which are formed the p_z electrons of graphene, are important for

understanding the band structure of graphene from theoretical calculations. In this section, the π band structure of graphene will be explained using tight-binding (TB) calculations [2, 3].

Let us solve the Schrödinger equation and define Bloch functions $\Phi_l(\mathbf{k})$ as

$$H\Psi(\mathbf{k}) = E(\mathbf{k})\Psi(\mathbf{k}), \quad (1.12)$$

$$\Psi(\mathbf{k}) = \sum_{l=A,B} C_l \Phi_l(\mathbf{k}) = \sum_{l=A,B} \sum_{\mathbf{R}_l} \frac{C_l}{\sqrt{N}} e^{i\mathbf{k}\cdot\mathbf{R}_l} \phi(\mathbf{r} - \mathbf{R}_l), \quad (1.13)$$

where $\phi(\mathbf{r} - \mathbf{R}_l)$ is a $2p_z$ orbital at the atom site coordinate \mathbf{R}_l for a carbon atom (A) and the nearest-neighbor carbon atom (B) of graphene. The reason why the tight-binding model can be applied is because the p_z orbital is perpendicular to graphene, which means the p_z wave function is localized.

Due to $C_l \neq 0$, we can obtain a secular equation as

$$\begin{vmatrix} H_{AA}(\mathbf{k}) - E(\mathbf{k})S_{AA}(\mathbf{k}) & H_{AB}(\mathbf{k}) - E(\mathbf{k})S_{AB}(\mathbf{k}) \\ H_{AB}^*(\mathbf{k}) - E(\mathbf{k})S_{AB}^*(\mathbf{k}) & H_{AA}(\mathbf{k}) - E(\mathbf{k})S_{AA}(\mathbf{k}) \end{vmatrix} = 0. \quad (1.14)$$

$$(H_{IJ} = \langle \Psi_I | H | \Psi_J \rangle, S_{IJ} = \langle \Psi_I | \Psi_J \rangle, \quad (I, J = A \text{ or } B).) \quad (1.15)$$

The solution to the equation is given by

$$E(\mathbf{k})^\pm = \frac{-(-2E_0 + E_1) \mp \sqrt{(-2E_0 + E_1)^2 - 4E_2E_3}}{2E_3}, \quad (1.16)$$

$$\begin{aligned} E_0 &= H_{AA}(\mathbf{k})S_{AA}(\mathbf{k}), & E_1 &= S_{AB}(\mathbf{k})H_{AB}^*(\mathbf{k}) + H_{AB}(\mathbf{k})S_{AB}^*(\mathbf{k}), \\ E_2 &= H_{AA}^2(\mathbf{k}) - H_{AB}(\mathbf{k})H_{AB}^*(\mathbf{k}), & E_3 &= S_{AA}^2(\mathbf{k}) - S_{AB}(\mathbf{k})S_{AB}^*(\mathbf{k}). \end{aligned} \quad (1.17)$$

In general, H_{AA} and S_{AA} are constants ($H_{AA} = \epsilon_{2p}$, $S_{AA} = 1$). On the other hand, we have to consider nearest-neighbor interaction in the case of H_{AB} and S_{AB} . They can be calculated as

$$H_{AB}(\mathbf{k}) = \gamma_0 \left(e^{-\frac{1}{3}i\mathbf{k}\cdot(\mathbf{a}_1+\mathbf{a}_2)} \right) \left(e^{i\mathbf{k}\cdot\mathbf{a}_1} + e^{i\mathbf{k}\cdot\mathbf{a}_2} + 1 \right), \quad (1.18)$$

$$S_{AB}(\mathbf{k}) = s_0 \left(e^{-\frac{1}{3}i\mathbf{k}\cdot(\mathbf{a}_1+\mathbf{a}_2)} \right) \left(e^{i\mathbf{k}\cdot\mathbf{a}_1} + e^{i\mathbf{k}\cdot\mathbf{a}_2} + 1 \right), \quad (1.19)$$

where γ_0 is called the carbon-carbon interaction energy and s_0 is overlap integral between K and K' points. Equation (1.16) therefore becomes

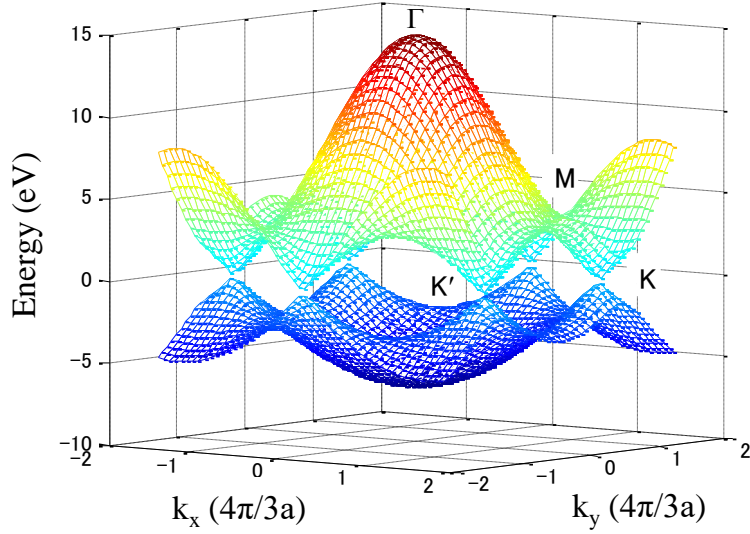


Figure 1.3: Band structure of graphene.

$$E(\mathbf{k})^{\pm} = \frac{\epsilon_{2p} \pm \gamma_0 \omega(\mathbf{k})}{1 \pm s_0 \omega(\mathbf{k})} \quad \text{and} \quad (1.20)$$

$$\omega(\mathbf{k}) = \sqrt{e^{ik_x a / \sqrt{3}} + 2e^{-ik_x a / 2\sqrt{3}} \cos \frac{k_y a}{2}}. \quad (1.21)$$

Finally, the band structure of graphene can be obtained as shown in Fig. 1.3.⁴ The upper energy band is the π anti-bonding band, and the lower one is the π bonding band. At K and K' points, there are no bandgap, so graphene behaves as semi-metal.

Band structure of single-walled carbon nanotubes

Brillouin zones of SWCNTs are the cutting lines as shown in Sec.1.1.1. The energy dispersion relations for SWCNTs are therefore given by using Eq.(1.21),

$$E_{\mu} = E \left(k \frac{\mathbf{k}_z}{|\mathbf{k}_z|} + \mu \mathbf{k}_{\perp} \right) \quad (1.22)$$

$$\left(\mu = 0, 1, \dots, N-1, \quad -\frac{\pi}{|\mathbf{T}|} \leq k \leq \frac{\pi}{|\mathbf{T}|} \right). \quad (1.23)$$

Figure 1.4 shows the Brillouin zones of (4,0), (5,0), and (6,0) nanotubes. Green lines indicate the nearest cutting line to the K point. In the case of (6,0) nanotubes, on the other hand, the cutting lines go through the K points, so the

⁴This Matlab code is shown in Ref [4]

SWCNT is metallic because the bandgap at the K point is zero. In the case of (4,0) and (5,0) tubes, these SWCNTs are semiconducting because these cutting lines do not cross the K point. It is known that SWCNTs can be classified by the following conditions [5, 6]⁵

$$n - m = 3l \quad (\text{metallic}), \quad (1.24)$$

$$n - m \neq 3l \quad (\text{semiconducting}). \quad (1.25)$$

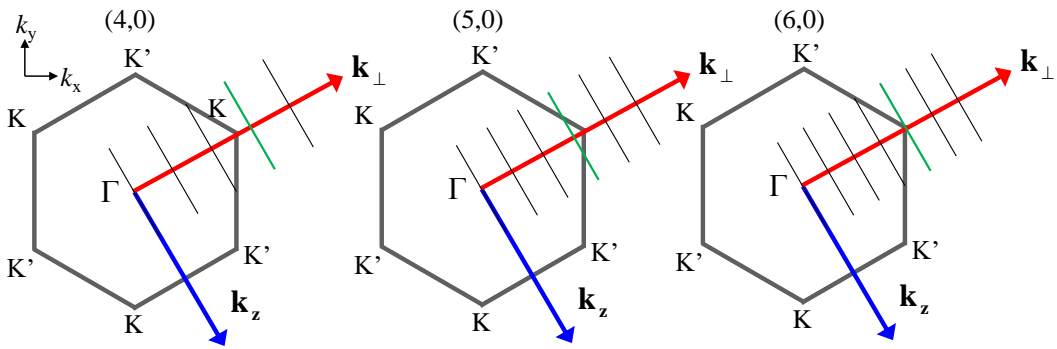


Figure 1.4: Brillouin zones of (4,0), (5,0), and (6,0) nanotubes (black and green lines).

1.1.3 Optical properties

Density of states and optical selection rules in single-walled carbon nanotubes

Due to the one dimensional structure of SWCNTs, the density of states (DOS) is very different from other bulk semiconductors. Figure 1.5 shows the DOS of semiconducting SWCNTs. Basically, the DOS of bulk semiconductor (three dimensional materials) is proportional to \sqrt{E} , but the DOS of SWCNTs has peaks at certain points. The DOS diverges asymmetrically, proportional to $1/\sqrt{E - E_i}$ (E_i is an external value). These divergent points are called van Hove singularities. When optical transitions occur between van Hove singularities, probability of the transition becomes very large due to the divergence of the DOS. c_i and v_i in Fig. 1.5 denote the van Hove singularities in the conduction bands and valence

⁵ l is integer.

bands, respectively. c_i and v_i are numbered in the order from the band gap, and E_{ij} denotes the gap energy between c_i and v_j .

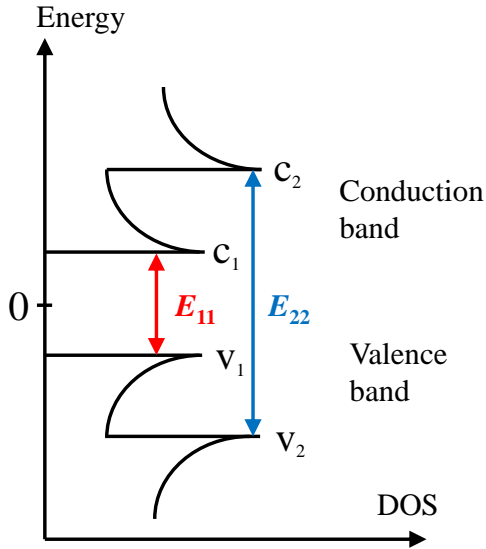


Figure 1.5: Density of states for a semi-conducting SWCNT.

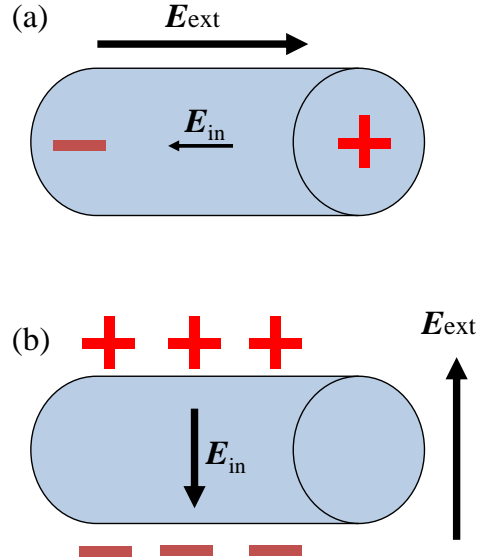


Figure 1.6: Schematics of polarized light (E_{ext}) parallel (a) and perpendicular (b) to tube axis. E_{in} indicates depolarization fields.

In addition, optical response of SWCNTs is different for the cases of parallel and perpendicular polarized beams to tube axis because of their one dimensional structure (Fig. 1.6). In the case of parallel polarized light, only $c_i v_i$ transitions (E_{ii}) occur. However, in the case of perpendicularly polarized light, $c_i v_{i\pm 1}$ transitions ($E_{i(i\pm 1)}$) are allowed. Moreover, the transitions caused by perpendicularly polarized light are suppressed since polarization generated in SWCNTs cancel out the optical electric field (depolarization effect) [7, 8]. There are several reports on absorption of perpendicularly polarized light, but the absorption is significantly smaller than that of parallel light (e.g. Ref. [9]). $c_i v_i$ transitions therefore dominate SWCNTs, and polarization dependence of PL shows $\cos^2 \theta$ [10].⁶

⁶ θ denotes electric field direction to tube axis. In the case of parallel and perpendicular polarized beams to tube axis, θ is 0° and 90°

1.1.4 Excitons and charged excitons in nanotubes

Semiconducting SWCNTs have a direct band gap (about 1 eV), and the DOS has van Hove singularities. Photoluminescence (PL) from SWCNTs can therefore be observed. In 2002, PL from micelle-wrapped SWCNTs was observed for the first time [11]. After this report, many optical properties of SWCNTs have been elucidated. One of the important properties is the excitonic effect which is described below.

Excitons in single-walled carbon nanotubes

Because of limited screening of Coulomb interaction in SWCNTs, an electron and a hole form tightly bound excitons which is analogous to a hydrogen atom.⁷ The excitonic effects were theoretically predicted in 1997 [13]. In 2005, the existence of excitons in micelle-wrapped SWCNTs has been demonstrated by two photon measurements [14,15], showing binding energies of 200-400 meV [Fig. 1.7]. Furthermore, the exciton binding energy of air-suspended tubes is found to become larger than that of micelle-wrapped tubes because of reduced dielectric screening effects [16]. Compared to the exciton binding energy of bulk materials such as GaAs⁸ (4.2 meV), excitons in nanotubes have significantly larger binding energy, and show unique optical properties as discussed below.

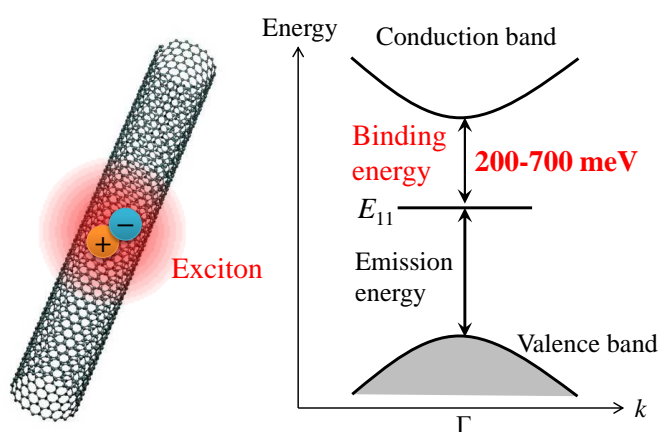


Figure 1.7: Excitons in carbon nanotubes.

⁷In the case of SWCNTs, the type of the exciton is Wannier-Mott [12].

⁸The bandgap energy is 1.42 eV at room temperature.

Bright and dark excitons in carbon nanotubes

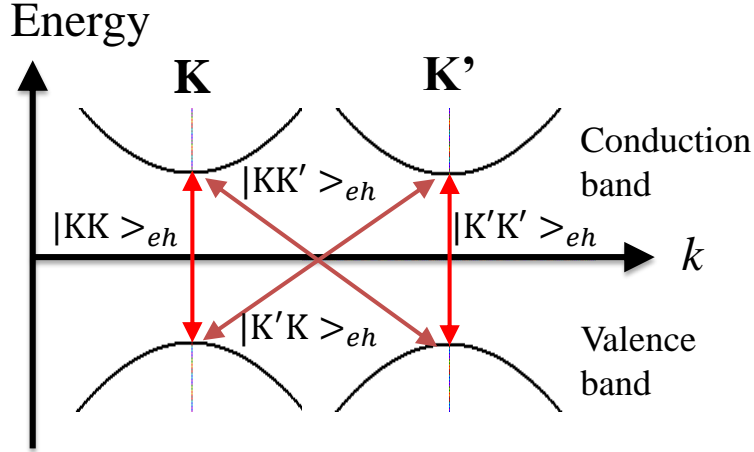


Figure 1.8: Band diagram of SWCNTs.

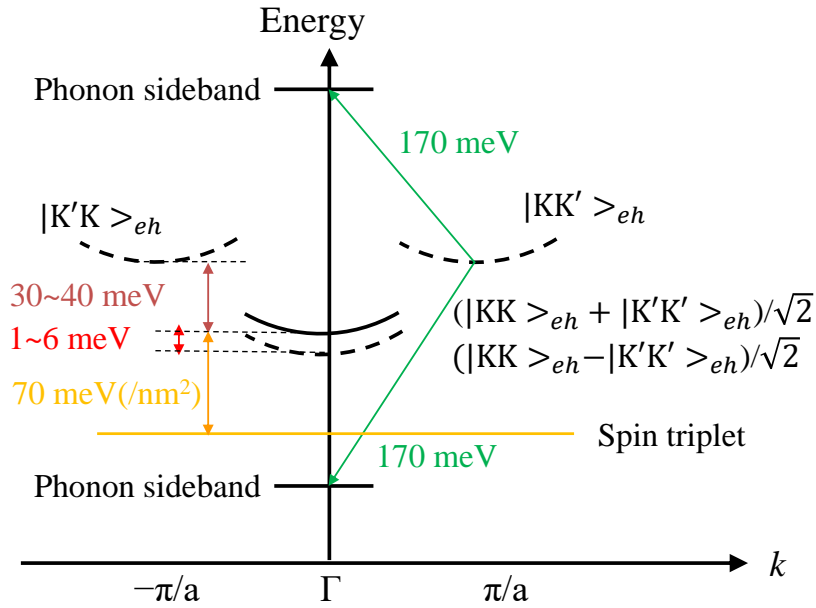


Figure 1.9: Energy diagram of E_{11} excitons in SWCNTs (about 1 nm diameter).

It is known that nanotubes have 16 types of excitonic states, and only one of them is optically active [17]. Because there are K and K' points, there are 4 combinations of an electron and a hole (Fig. 1.8) Moreover, electrons and holes have 2 possible spin states (up and down). As a result, there are 16 types of

excitons ($4 \times 2 \times 2$). Spin singlet and triplet states are represented as

$${}^S |v, v'\rangle_{eh} = \frac{1}{\sqrt{2}} (|(v, \uparrow)(v', \uparrow)\rangle_{eh} + |(v, \downarrow)(v', \downarrow)\rangle_{eh}) \quad (\text{spin singlet}), \quad (1.26)$$

$${}^{T0} |v, v'\rangle_{eh} = \frac{1}{\sqrt{2}} (|(v, \uparrow)(v', \uparrow)\rangle_{eh} - |(v, \downarrow)(v', \downarrow)\rangle_{eh}) \quad (\text{spin triplet}), \quad (1.27)$$

$${}^{T+} |v, v'\rangle_{eh} = |(v, \uparrow)(v', \downarrow)\rangle_{eh} \quad (\text{spin triplet}), \quad (1.28)$$

$${}^{T-} |v, v'\rangle_{eh} = |(v, \downarrow)(v', \uparrow)\rangle_{eh} \quad (\text{spin triplet}), \quad (1.29)$$

where v and v' correspond to K- and K'-states of a electron (e) and a hole (h), respectively.⁹ The 16 types of excitons are expressed as

$${}^i |KK \pm K'K'\rangle_{eh} = \frac{1}{\sqrt{2}} ({}^i |KK\rangle_{eh} \pm {}^i |K'K'\rangle_{eh}), \quad (1.30)$$

$${}^i |KK'\rangle_{eh}, \quad \text{and} \quad {}^i |K'K\rangle_{eh}, \quad (1.31)$$

where i denotes S, T0, T+, or T-. Because the conditions for being optically active are zero angular momentum, odd parity, and spin singlet, only one type of excitons satisfies these conditions (bright exciton, ${}^S |KK + K'K'\rangle_{eh}$ ¹⁰). In contrast, other 15 types of excitons are optically forbidden, and therefore they are called dark excitons.

Some of the dark excitons can be observed, however, in optical measurements directly or indirectly. Ando predicted Aharonov Bohm (AB) effects in SWCNTs [7, 18], which means that spin-singlet zero-momentum dark excitons (${}^S |KK - K'K'\rangle$) can become optically-active by breaking time-reversal symmetry. In fact, AB effects were observed, and the energy splitting between the dark state and the bright state of E_{11} excitons was found to be about 1-6 meV [19–22].

In addition, singlet KK' and $K'K$ states of E_{11} excitons were revealed indirectly [23–25]. Basically, these states are not optically-active, but the energy level above and below ~ 170 meV from KK' and $K'K$ states can emit light by exciton-phonon interaction, which is called K-momentum dark exciton (phonon sideband). From the experimental results, the energy difference between the bright state and KK' ($K'K$) state is found to be about 30-40 meV.

⁹Please note that the spin of a hole is opposite to notations used frequently in quantum mechanics textbooks because of the charge difference between a hole and a electron.

¹⁰+ means bonding state. On the other hand, - means anti-bonding state

Spin triplet states have also been observed despite being dark states [26–28]. It is considered that the mechanism of being optically active is due to mixing between the wave function of the triplet state and the bright states, and this energy depends on the diameter of SWCNTs (70 meV/nm^2). In Fig. 1.9, we show an energy diagram of E_{11} excitons in SWCNTs.

Trions (charged excitons) in nanotubes

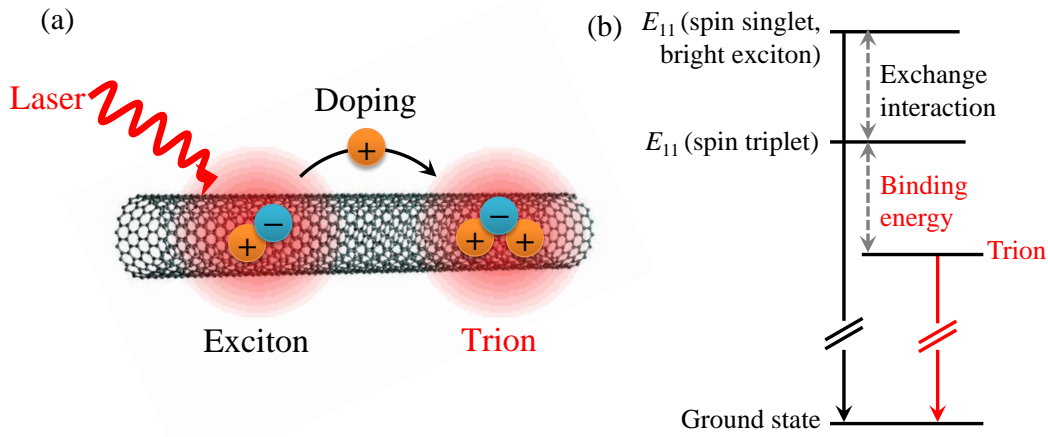


Figure 1.10: (a) Excitons and trions (or charged excitons) in a carbon nanotube. (b) A schematic of the energy levels of the singlet excitons, triplet excitons, and trions.

Because of the limited screening of Coulomb interaction in one-dimensional systems, it has been theoretically predicted that a charged carrier can be bound to an exciton to form a trion (or a charged exciton) in nanotubes [Fig. 1.10(a)] [29], similar to a hydrogen ion atom (H^-) or an ionized hydrogen molecule (H_2^+) [30]. As trions possess both charge and spin, they have received considerable attention in spintronics and quantum information [31]. Experimentally, tightly bound trions in micelle-wrapped nanotubes have been observed under chemical doping [32] or by all optical generation [33] in 2011. By comparing these experimental results with theory [29, 34–36], it is confirmed that the trion emission originates from a bound state of a triplet exciton and a charged carrier [Fig. 1.10(b)]. Furthermore, the trion binding energy is found to be 49–85 meV in the case of 1-nm diameter tubes, which means that trions in nanotubes are stable even at room temperature. Similar to excitons in nanotubes, such a system with large trion binding energies

is distinct compared to other bulk or low-dimensional materials,¹¹ and therefore investigating the optical properties of trions is important for understanding of many-body effects caused by Coulomb interaction in low-dimensional systems.

1.2 Carbon nanotube optoelectronics

1.2.1 Advantages and unique characteristics

As introduced in Sec. 1.1, SWCNTs are quasi one-dimensional nano-materials with diameters of 1-3 nm and lengths of >100 nm. In the case of semiconducting tubes, they have a direct bandgap and show telecom-band emission [11]. In addition, nanotubes can be directly synthesized on silicon substrates [39], and electrodes can be attached by microfabrication technology [40, 41]. SWCNTs are therefore promising materials for optoelectronic devices at the nanoscale [42].

Excitonic effects in nanotubes dominate optical transitions, however, with large binding energies due to limited screening (Sec. 1.1.4) [14–16], and it is often difficult to apply common methods used for other bulk semiconductors, resulting in insufficient understanding of the optical properties of nanotubes. Their electronic structure are also dependent on chirality [43–45] and surrounding ambient [16, 46–49]. Because of such unique characteristics of carbon nanotubes, understanding of electric field effects on excitons in nanotubes is important for applications in optoelectronics.

1.2.2 Previous works on electric field effects on excitons in nanotubes

Here we review some previous works that discuss electric field effects on excitons in nanotubes from theoretical or experimental approaches. For experiments, we focus on electroabsorption, photocurrent, and photoluminescence, while there are many other studies such as electrically-driven light emission [50–54], Rayleigh scattering spectroscopy [55], Raman spectroscopy [56, 57], and scanning tunneling

¹¹Trion binding energies of quantum wells (CdZnTe/CdTe/CdZnTe) [37] and transition metal dichalcogenide monolayers (MoS₂) [38] are 1-5 meV and 20-30 meV, respectively.

microscopy [58].

Theoretical approaches

The electro-optical response of carbon nanotubes has been studied theoretically by V. Perebeinos and P. Avouris [59]. They predicted the chirality-dependent change in absorption spectrum of SWCNTs under electric fields parallel to the nanotube axis, which is caused by Franz-Keldysh effect, Stark effect, and exciton dissociation. Furthermore, such theoretical studies have been performed in the case of electric fields applied in the longitudinal [60] or perpendicular [61] directions with respect to nanotube axis, showing modulations of excitonic optical properties in nanotubes. Those works have considered only pure external electric fields, while electrostatic doping causes tuning of the bandgap energies [62]. When investigating electric field effects on excitons in nanotubes experimentally, it is therefore important to consider various effects caused by chirality, field directions, and carrier doping.

Electroabsorption

As electro-optic modulators, electroabsorption measurements have been conducted using carbon nanotube thin film transistors, and small redshifts has been observed due to Stark effect [63]. In spite of samples with mixed chirality in ensembles,¹² electroabsorption measurements have shown Franz-Keldysh oscillation [64], terahertz electro-optic modulation [65], and existence of dark excitonic states [66].

Photocurrent

Carbon nanotube field-effect transistors (FETs) can act as a nanoscale polarized photodetector [67] and an optoelectronic digital-analog converter [68], and therefore the electro-optical response characteristics of nanotubes need to be understood. Photocurrent measurements have demonstrated band-gap renormal-

¹²In the case of absorption measurement, the sample size should be comparable or larger compared to spot size of excitation light.

ization [69], multiple exciton generation [70], existence of dark excitonic states [26, 71], photocurrent quantum yield [72, 73], ultrafast optical response [74], exciton dissociation [75], and Stark effect of excitons [75]. However, the mechanism of photocurrent generation in semiconducting tube is complex [76–80] because of mixed photovoltaic effects induced by a built-in electric field [76, 79–82] and photothermal effects [77, 78, 83].

Photoluminescence

Since semiconducting SWCNTs show emission in the telecommunication wavelengths, nanoscale electrical-to-optical (E/O) devices would be feasible using nanotubes. Previously, interactions between excitons and free carriers using nanotube FETs has been investigated by PL measurements [57, 84–88]. Bias [84–86] or gate [57, 87] voltages induce quenching of photoluminescence, which may be caused by Auger process [89, 90], band-filling, screening, and formation of trions [91]. It is, however, difficult to explain the behavior that PL intensity decreases exponentially with gate voltage by these mechanisms [87]. Despite the unknown mechanism of PL quenching, intensity can be easily controlled with low gate voltages, and Ref. [88] has showed E/O signal conversions at high frequency. In addition to PL intensity modulation, slight blueshifts have been observed with an application of gate voltages [87]. According to a theoretical paper [62], the energy shifts of E_{11} excitons may be caused by a combination of band-gap renormalization, band-filling, and exciton renormalization [Fig. 1.11]. In total, E_{11} energy shifts are almost cancelled by these effects, but slight blueshifts are predicted with increasing doping concentration.

So far, we have discussed electrical response on excitons in nanotubes, while trion generation by a combination of electrical and optical methods is also one of the interesting topics for carbon nanotubes. Electrochemical doping methods [92] have demonstrated emission from negative trions and positive trions. Since the trion peak emerges with increasing electrochemical potential voltage, E/O signal conversions are allowed using trions as for excitons in nanotubes.

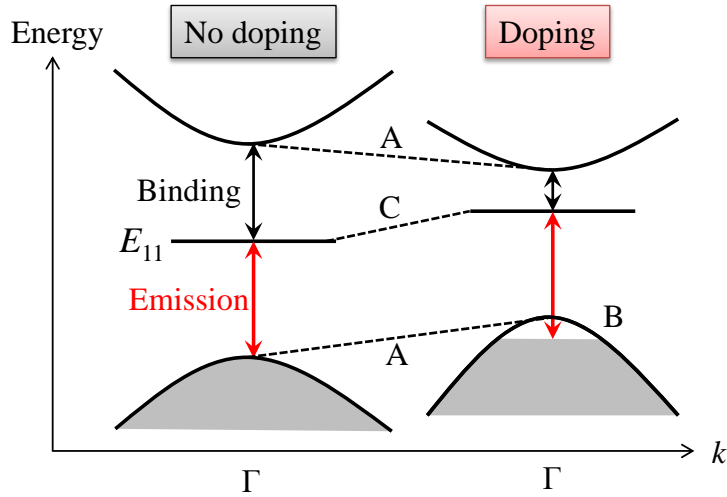


Figure 1.11: Illustration of renormalization of band-gap and exciton binding energies in a carbon nanotube. Right and left figures show the band structures of the tube with and without doping, respectively. A, B, and C correspond to effects on band-gap renormalization, band filling, and exciton renormalization, respectively. Reduction in the band-to-band continuum and exciton binding energies are caused by screening when carriers are doped.

1.2.3 Issues and difficulties

Many works explained in the previous subsection have investigated electric field effects on excitons in carbon nanotubes, but experimental studies on chirality dependence of these effects are sparse, being an open question. Although electronic structure of nanotubes depends on chirality [43–45], it is difficult to control chirality using common synthesis methods, and therefore as-grown ensemble samples typically contain mixed-chirality nanotubes. In this case, ensemble samples show multiple broad peaks in spectra, making it difficult to analyze weak side peaks and chirality dependence of energy shifts (e.g. Ref. [63, 66, 85]). Recently, methods for chirality separation [93] and single-chirality nanotube growth [94, 95] have been developed in order to obtain single-chirality SWCNTs. However, it is still difficult to analyze slight energy shifts using single-chirality ensembles (e.g. [91]) due to inhomogeneous broadening [96].

Another approach is to perform measurements using individual carbon nanotubes. They have clear single peaks and narrow linewidth in spectra compared to ensembles. Individual samples therefore provide information on intrinsic prop-

erties of nanotubes, and discussions on slight energy shifts and small peaks in the spectra are possible (e.g. Ref. [75]). Chirality identification is, however, non-trivial, and nanotubes with unknown chirality make it difficult to perform quantitative analysis and to compare experimental data with theory. In order to determine the chirality, scanning tunneling microscopy [97] and electron diffraction [98] have been used, but these measurements are difficult or destructive.

1.3 Research objective

The purpose of this dissertation is to elucidate electric field effects on excitons in SWCNTs, and we perform measurements on chirality-assigned individual nanotubes to address issues caused by chirality dependent band structure. In this work, we perform PL measurements, and PL excitation (PLE) spectroscopy allows determination of chirality (Fig. 1.12) [43, 47, 99]. Furthermore, PL measurements make in-situ experiments possible and are non-destructive in contrast to scanning tunneling microscopy and electron diffraction.¹³

For this research objective, we have fabricated individual suspended nanotube FETs, and have constructed a confocal microscope system. For the device fabrication, we have prepared clean pristine nanotubes by synthesizing nanotubes at the final stage of the fabrication process. In this manner, we can characterize intrinsic optical properties of nanotubes. By optimizing the nanotube growth conditions, we can also control the diameter distribution of nanotubes, and they typically have emission wavelengths within the detection range of InGaAs detectors, making chirality assignment possible. For the optical setup, laser wavelength, power, polarization, and sample position (or laser spot) are mostly automated, so that we are able to collect large amounts of data efficiently. Furthermore, we monitor photocurrent as well as PL in order to quantitatively evaluate exciton dissociation and exciton recombination.

¹³Recently, photocurrent excitation spectroscopy [72, 73, 100] also enables to identify chiralities.

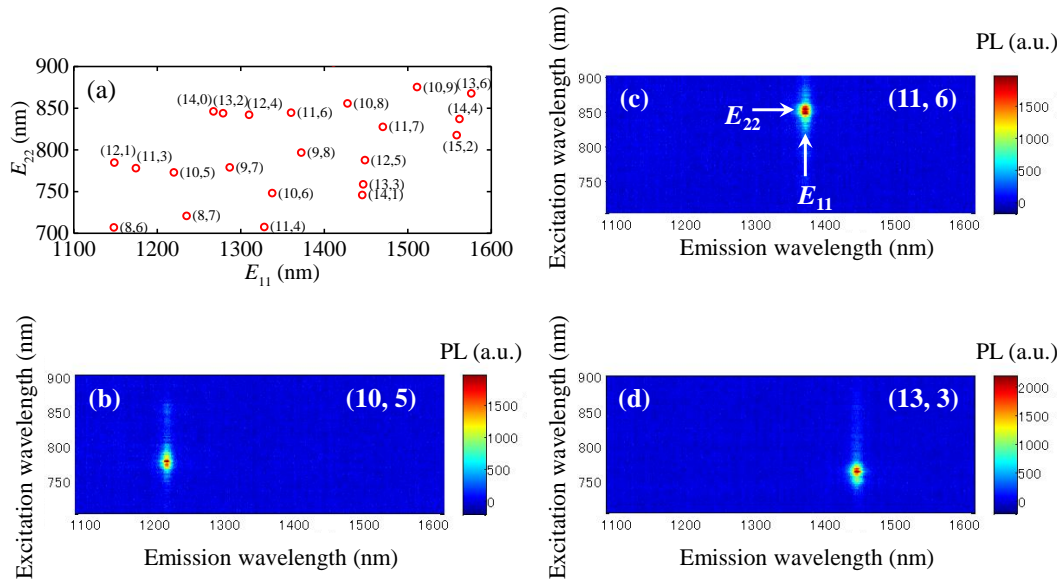


Figure 1.12: (a) Average E_{11} and E_{22} peak positions for individual air-suspended carbon nanotubes, based on Ref. [99]. (b-d) Typical PLE maps of individual (10,5), (11,6), and (13,3) suspended nanotubes, respectively. By taking PL spectra as a function of excitation wavelength, E_{11} and E_{22} wavelengths are determined (see also Sec. 1.1.3).

1.4 Organization

This dissertation is organized as follows. In Chap. 2, the device fabrication process of carbon nanotube FETs used to investigate electric field effects on excitons in individual SWCNTs is described. Next, simultaneous photoluminescence and photocurrent measurements with an application of bias voltage is presented in Chap. 3. We find that excitons are spontaneously dissociating into free electron-hole pairs (Sec. 3.2, [101]), and the Stark-effect induced redshifts of PL show quantitative agreement with theoretical calculations (Sec. 3.3, [102]). Furthermore, gate-voltage dependence of PL in individual suspended tubes shows an emergence of trion emission due to electrostatic doping, and this is presented in Chap. 4 [103].

Chapter 2

Carbon nanotube field effect transistors

In order to perform optical measurements on individual suspended SWCNTs under electric fields, we have fabricated suspended carbon nanotube field-effect transistors.

2.1 Sample description

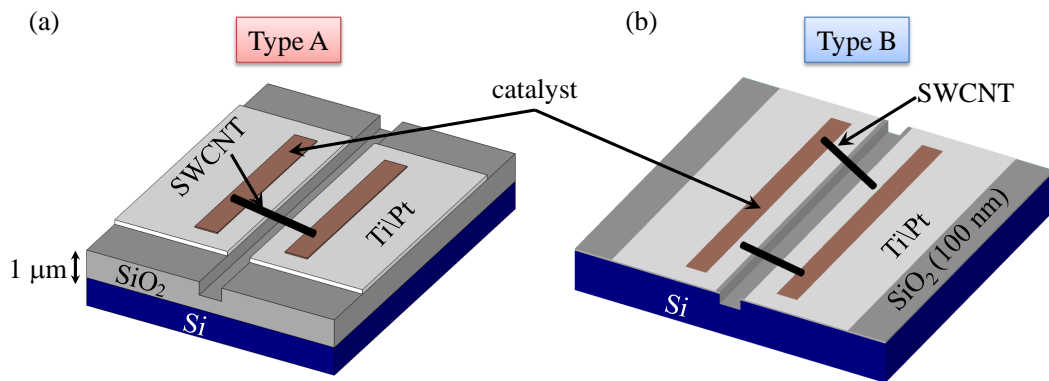


Figure 2.1: (a-b) Schematic of type A and type B devices, respectively. Type A devices are used for Chap. 3.3, while type B devices are utilized in Chap. 4.

Figure 2.1 shows device schematics of carbon nanotube field-effect transistors (FETs). Type A devices [Fig. 2.1(a)] are used for simultaneous PL and PC measurements under bias voltage application in Chap. 3.3, while type B devices [Fig. 2.1(b)] are designed for PL measurement with gate voltages in Chap. 4. Sample layouts are designed using LayoutEditor software as shown in Fig. 2.2,

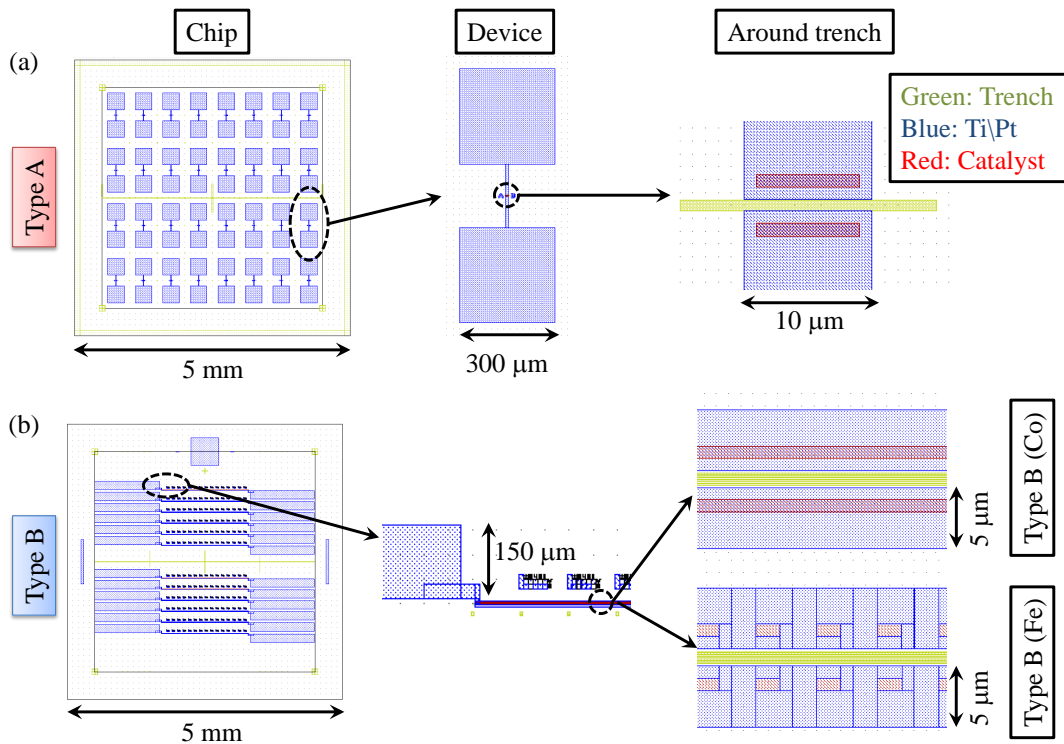


Figure 2.2: (a-b) Sample layouts of type A and type B devices, respectively. For type A and type B (Co), catalyst region (red) is placed on Ti\Pt electrodes (blue). In contrast, catalyst region is not overlaid with Ti\Pt region in the case of type B (Fe).

Table 2.1: Information of wafers and device parameters.

	Type A	Type B
Dopant	boron (<i>p</i> type)	boron (<i>p</i> type)
Si resistivity	15 ± 5 m Ω cm	15 ± 5 m Ω cm
SiO ₂ thickness	1 μ m	100 nm
Trench width	1.0-1.7 μ m	0.4-1.6 μ m
Trench length	10 μ m	1600 μ m
Backset	50 nm	200-1000 nm

and description of wafer and device parameters is summarized in Table 2.1. The main differences between type A and B are the thickness of SiO₂ layer, trench width, and backset.¹ For type A, we use a Si substrate with 1 μ m-thick oxide in order to prevent gate-induced carrier doping, and a trench length is only 10 μ m because additional dark current from other nanotubes when performing PC mea-

¹Distance between the Ti\Pt electrode and the edge of the trench.

surement needs to be suppressed.² In contrast, type B devices have 100-nm-thick oxide layer in order to perform carrier doping efficiently by applying gate voltages,³ and we use 1.6-mm-long trenches which allow numerous SWCNTs to be suspended. Furthermore, the backset of type A is designed to be 200-1000 nm in order to avoid overlaps between electrode and trench patterns, which may arise due to charging effects or misalignments in electron beam lithography.⁴

In Fig. 2.2(b), we note that the Co/silica catalyst is placed on top of the Pt electrodes (Type B (Co)), while the Fe-thin film catalyst covers the SiO₂ area in small windows opened up within the electrodes (Type B (Fe)). This is because SWCNTs do not grow from Fe-thin film on Pt (Appendix A).

2.2 Device fabrication

Such devices described in Sec. 2.1 have been fabricated using microfabrication techniques. In order to grow clean suspended SWCNTs, growth has been performed after trench formation and metal deposition (Fig. 2.3). We note that alignment marks are needed in type A devices before formation of trenches, and the detailed fabrication processes of type A are described in Ref. [104].

Formation of trenches and annealing

First, we perform spin-coating of OAP at 3000 rpm for 30 s on Si substrates with an oxide layer, and then OEBR CAP-112PM resist is spin-coated at 2500 rpm for 60 s, followed by baking at 110°C for 5 min on a hot plate.⁵ In order to pattern trenches, electron-beam lithography (ADVANTEST, F5112) is performed with a dose amount of 7 $\mu\text{C}/\text{cm}^2$, and the exposed chips are baked at 110°C for 2 min. The chips are developed by tetramethyl ammonium hydroxide

²One nanotube per device is desirable.

³The capacitance is inversely proportional to the oxide layer thickness.

⁴For type A, the backset is designed to be 50 nm, but a part of Pt film is attached to a sidewall of a trench as observed in Fig. 2.5(a). In this case, electrostatic gating to SWCNTs may be inefficient compared to type B devices as shown in Fig. 2.5(b) because most of electric force lines is expected to be absorbed from the Si substrate to the Pt film at the sidewall.

⁵Chip sizes are 30×30 mm² and 26×26 mm² for type A and B, respectively.

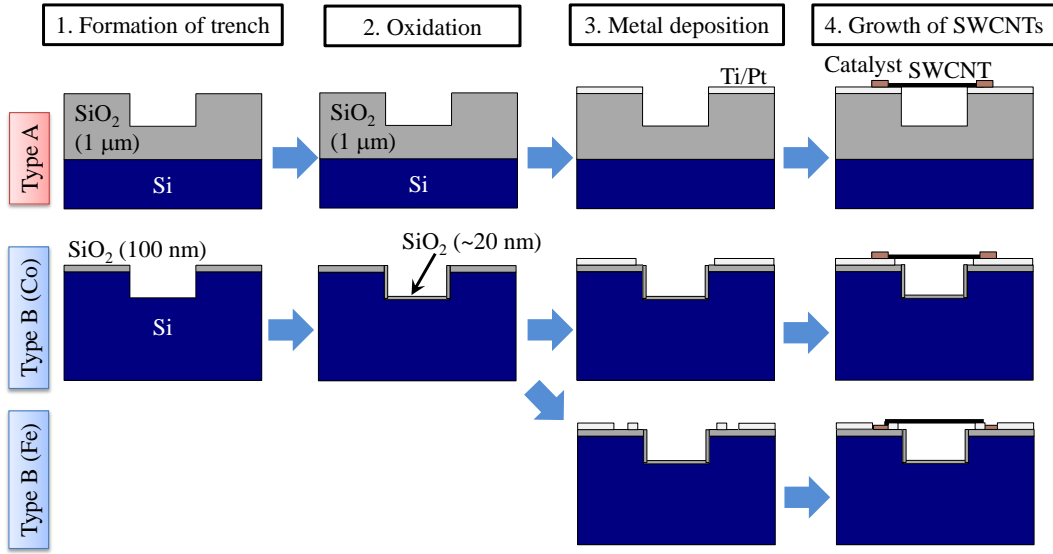


Figure 2.3: Device fabrication processes for type A and type B devices.

(TMAH) for 1 min, and are rinsed in water. After baking at 110°C for 1-2 min, the patterned samples are dry-etched by inductively coupled plasma (ICP) using CHF₃ gas, forming 500-nm-deep trenches. Following the etching process, the resist on the chips is removed by Hakuri104 (Tokyo Ohka Kogyo) with sonication for 10 min,⁶ and the chips are cleaned by isopropyl alcohol (IPA). The samples are then oxidized in an annealing furnace at 900°C for an hour in order to form a 20-nm-thick SiO₂ layer in the trenches. The annealing also burns out the residual resist and prevents gate leakage in devices. In Table 2.2, the process conditions for trench formation and annealing are summarized.

Metal deposition

Next, spin-coating using OAP is done on the chips at 4000 rpm for 60 s, and ZEP520A resist is spin-coated with the same condition. The chips are pre-baked at 180°C for 10 min, and another electron-beam lithography step with a dose amount of 104-120 $\mu\text{C}/\text{cm}^2$ defines the electrode patterns. Using an electron beam evaporator (ULVAC, EX400) with a base pressure of 1×10^{-4} Pa, we deposit Ti (3 nm)\Pt (45 nm) or Ti (2 nm)\Pt (20 nm) for type A or B devices,

⁶When the resist removal is not enough, the chips are soaked in acetone for 5 min with sonication.

Table 2.2: Summary of fabrication process (trench formation and annealing).

	Process	Item	Condition	
			Type A	Type B
0	Alignment mark		Ref. [104]	-
1	Resist coating	OAP	500 rpm, 5 s	"
			3000 rpm, 30 s	"
2	Resist coating	OEBR- CAP112PM	500 rpm, 5 s	"
			2500 rpm, 60 s	"
3	Prebake	Hot plate	110°C, 5 min	"
4	E-beam lithography	ADVENTEST F5112	7 $\mu\text{C}/\text{cm}^2$	"
5	Post bake	Hot plate	110°C, 2 min	"
6	Development	TMAH 2.38%	1 min	"
7	Rinse	Water	1 min \times 3	"
8	Bake	Hot plate	110°C, 1 min	110°C, 2 min
9	ICP etching	ULVAC CE-300I	CHF ₃ , 0.5Pa, RF:150 W, 200 s	CHF ₃ , 0.5Pa, RF:38 W, 15 min
10	Resist removal	Hakuri104	10 min (sonication)	"
11	Resist removal	Acetone	-	5 min (sonication)
12	Rinse	IPA	1 min \times 2	"
13	O ₂ annealing	Annealing furnace	O ₂ :1.5 L/min, 900°C, 1 hour	"

respectively. We note that high temperature vacuum grease (Apiezon H) is spread on the back side of the chips before sample setting, preventing hardbake of resist during evaporation. After the metal deposition, the resist is removed by soaking in Hakuri104 for 1 day and sonication for 5 min, and then the samples are rinsed in IPA.⁷ Furthermore, in order to clean up the surface of the substrates, O₂ plasma ashing (SAMCO FA-1) is conducted, and then sonication in acetone for 5 min is performed. In Table 2.3, these process conditions are summarized.

Growth of carbon nanotubes

Following the lift-off process for the contacts, catalyst windows near the trenches are patterned with a third electron beam lithography step. The chips

⁷For type B, additional sonication for 15 min is performed.

Table 2.3: Summary of fabrication process (metal deposition).

	Process	Item	Condition	
			Type A	Type B
14	Resist coating	OAP	500 rpm, 5 s 4000 rpm, 60 s	
15	Resist coating	ZEP520A	500 rpm, 5 s 4000 rpm, 60 s	
16	Prebake	Hot plate	180°C, 10 min	
17	E-beam lithography	ADVENTEST F5112	104-120 $\mu\text{C}/\text{cm}^2$	
18	Development	ZED-N50	1 min	
19	Rinse	ZMD-B	1 min \times 2	
20	E-beam evaporation	ULVAC EX400	Ti (3 nm) Pt (45 nm) 0.1 nm/s $1 \times 10^{-4}\text{Pa}$	Ti (2 nm) Pt (20 nm) 0.04 nm/s "
21	Lift off	Hakuri 104 (different) Hakuri104	RT, 1 day 5 min (sonication) -	70°C, 1 day " RT, 15 min (sonication)
22	Rinse	IPA	1 min \times 2	"
23	O ₂ plasma ashing	SAMCO FA-1	5 min	10 s
24	Cleaning	Acetone	5 min (sonication)	"

are then divided into $5 \times 5 \text{ mm}^2$ chips using stealth dicing technology (DISCO DFL7340). Catalyst solution for nanotube growth is prepared by ultrasonically dispersing 5 mg of cobalt(II) acetate tetrahydrate and 25 mg of fumed silica in 10.0 g of ethanol [102], and then we perform spin-coating and lift off the catalyst. We note that we use thermally evaporated Fe-thin films [105] in some type B devices in order to grow SWCNTs with a wide diameter range.⁸ After the lift-off process, the chips are heated in a muffle furnace in air for 5 min at 400°C. Finally, SWCNTs are synthesized by chemical vapor deposition (CVD) [106,107] at 800°C with a growth time of 10 min and 1 min in the case of type A and B devices,

⁸We utilize a small vacuum evaporator (ULVAC VPC-260F), and Fe-thin film is deposited with the thickness of 0.2 nm. We use an Fe wire (Niraco FE-221480) and a tungsten boat (Niraco SV207W) when performing deposition. We also note that lift-off condition of Fe film is different from that of Co/silica catalyst (30' in Table 2.4).

respectively.⁹ Ethanol is introduced as a carbon source by bubbling H₂/Ar gas.

Table 2.4: Summary of fabrication process (growth of carbon nanotubes).

	Process	Item	Condition	
			Type A	Type B
25	Same as 14~19			
26	Dicing	DISCO DFL7340		
27	Catalyst preparation		Ethanol: 10 g	"
			Co:5 mg	"
			Silica: 25 mg	"
28	Catalyst spin-coating	Catalyst	3000 rpm, 50 s	5000 rpm, 50 s
28'	Fe catalyst deposition	ULVAC 260F	VPC-	Fe: 0.2 nm
29	Bake	Hotplate	150°C, 5 min	100°C, 5 min
30	Lift off	Hakuri 104	RT, 15 min [104]	70°C, 60 min [108]
30'	Lift off (Fe)	Hakuri 104	-	15 min (sonication)
		Acetone	-	10 min (sonication)
31	Rinse	IPA	1 min × 2	"
32	Heating	Furnace	400°C, 5min	"
33	CVD	CVD	800°C, 10 min	800°C, 1 min
			Ethanol, Bubbling	"

Figures 2.4 and 2.5 show optical microscope images and scanning electron microscope (SEM) images, respectively. As shown in the SEM images, carbon nanotubes are suspended over trenches.

⁹For type A, before CVD process, the samples are placed in a quartz tube furnace and heated in dry air while the temperature is ramped up to 700°C over 12 min. After pumping out the dry air, the quartz tube is filled by Ar with 3% H₂, and the temperature in the furnace is elevated to 800°C.

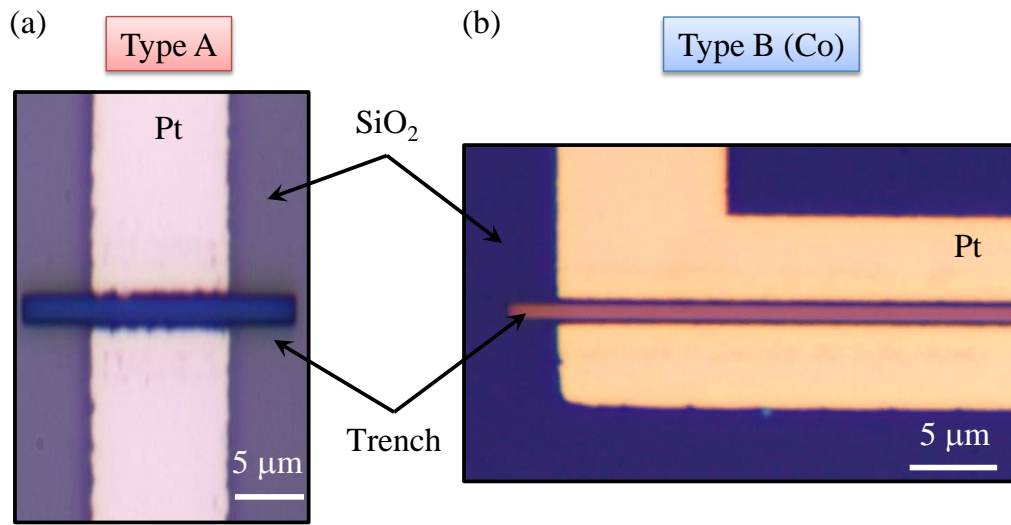


Figure 2.4: (a-b) Top-view optical microscope images of type A and type B devices, respectively.

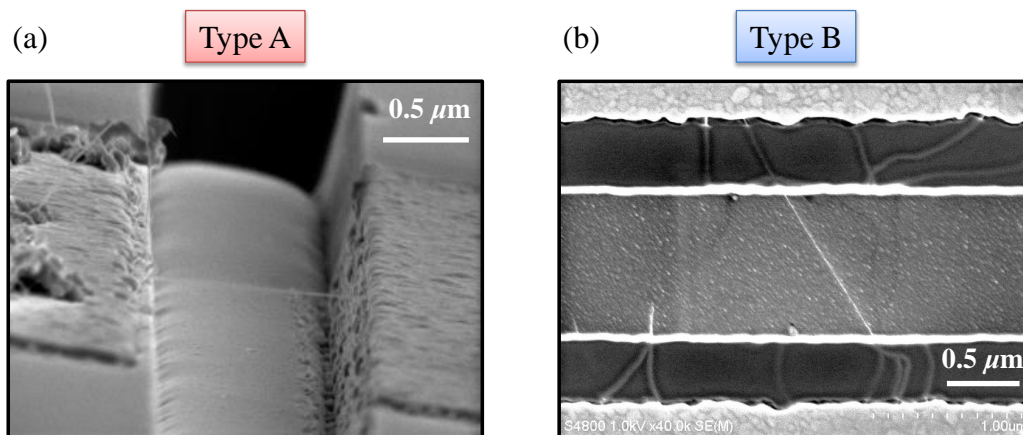


Figure 2.5: (a) A side-view scanning electron micrograph of a type A device with a trench width of 1.3 μm. Original data presented in Ref. [101]. (b) Top view of a scanning electron micrograph image of a type B device. A trench width and a backset are designed to be 1.0 μm and 0.5 μm, respectively.

Chapter 3

Bias voltage effects on excitons in individual suspended carbon nanotubes

3.1 Simultaneous photoluminescence and photocurrent measurements

3.1.1 Background on bias voltage effects on excitons in nanotubes

Now we investigate bias voltage effects on excitons in nanotubes using type A devices as described in Chap. 2. Perebeinos *et al.* have predicted exciton dissociation and Stark effect on excitons in nanotubes under electric fields [59], and quantitative analyses on these effects would be possible by performing simultaneous PL and PC measurements [Fig. 3.1]. However, it has been demonstrated that PL is quenched by an application of bias voltage [57, 84–86], making the simultaneous PL and PC measurements difficult. Because strong electric fields on the order of $100 \text{ V}/\mu\text{m}$ is necessary for exciton dissociation [59, 86], the PL quenching may be caused by carrier injection effects such as band filling, screening, and Auger recombination [86, 87]. In order to suppress the carrier injection with bias voltages, symmetric bias voltage application is useful [101, 102], and this method allows measurements with purely longitudinal electric fields.

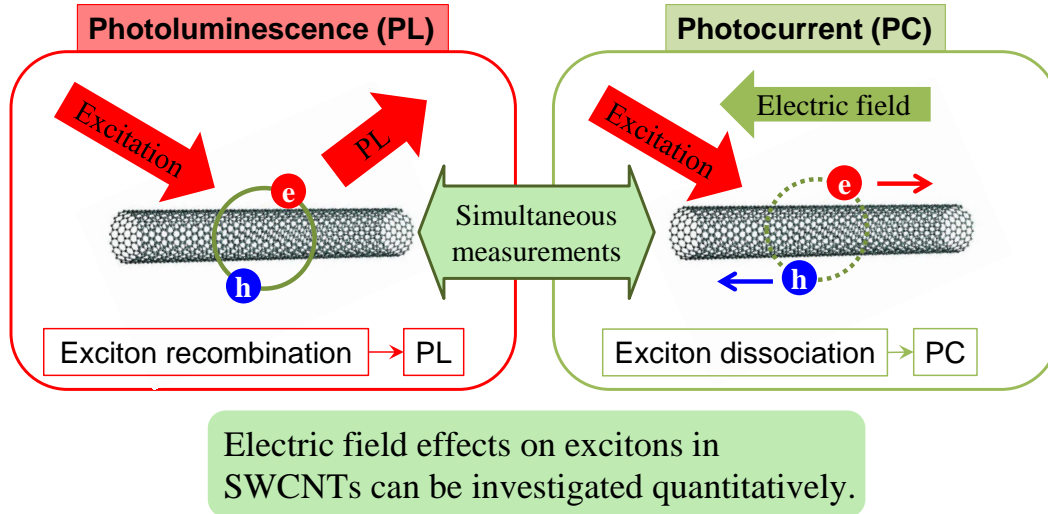


Figure 3.1: Simultaneous photoluminescence and photocurrent measurements.

3.1.2 Optical setup

The type A devices are characterized with a confocal micro-PL measurement system optimized for detection of nanotube emission as shown in Fig. 3.2 [99]. An output of a wavelength tunable Ti:sapphire laser is focused onto the sample by an objective lens with a numerical aperture (NA) of 0.8 and a working distance of 3.4 mm. PL is collected through a confocal pinhole corresponding to an aperture with $5.4 \mu\text{m}$ diameter at the sample image plane. An InGaAs photodiode array and a spectrometer with a spectral resolution of $\sim 1 \text{ meV}$ are used to detect PL from nanotubes. We utilize an automated three-dimensional translation stage with a travel range of $\pm 10 \text{ mm}$ and a resolution of 50 nm to take PL images and to find the nanotube positions. PL excitation spectroscopy is performed to determine the chiralities of individual SWCNTs using tabulated data for air-suspended tubes [47]. The nanotube length can be calculated from the width of the trench and the tube angle obtained from laser polarization dependence of PL [109].

Simultaneous PL and PC measurements are performed in the presence of electric field using two dc source meters (ADCMT, 6241A). We apply voltages $\pm V/2$ to the source and drain contacts, respectively, and ground the Si substrate [Fig. 3.3(a-b)] in order to avoid PL quenching caused by carrier-induced Auger

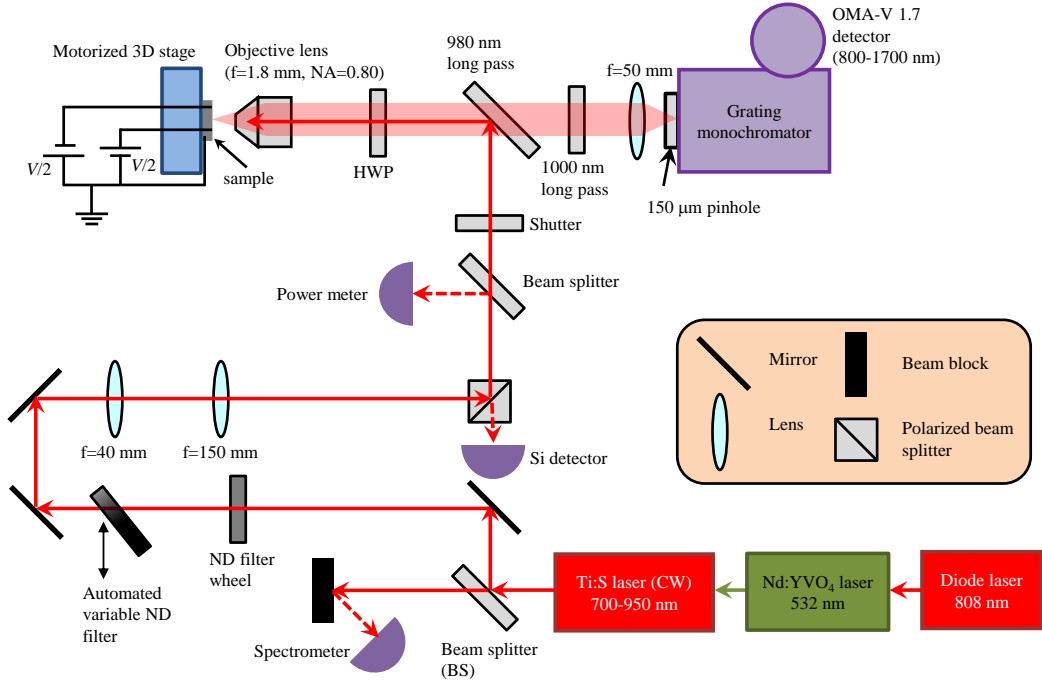


Figure 3.2: A schematic of an optical setup.

recombination [86,87]. The longitudinal component of electric field F is obtained by dividing the applied voltage with the tube length. We average the current with the excitation laser on the sample while a spectrum is taken, and then a background spectrum and a dark current are collected after blocking the laser with a shutter. The PL spectrum is obtained by taking the difference of the two spectra. All measurements are done in air at room temperature.

3.1.3 Imaging

Figure 3.3(c) is an optical microscope image of the device, and in the area indicated by the black box, we perform reflectivity, PL, and PC imaging simultaneously at an excitation laser power $P = 15 \mu\text{W}$. The reflectivity image [Fig. 3.3(d)] shows the position of the trench, and a luminescent nanotube suspended over the trench can be seen in the PL image [Fig. 3.3(e)]. The PC image shows that the signal is maximized at the same spot as PL [Fig. 3.3(f)]. In contrast to the case of Schottky barrier imaging [82,110–112], we do not observe PC when the laser spot is near or on the contacts. This confirms that band bending and electrostatic doping near the contacts are negligible in our voltage configuration.

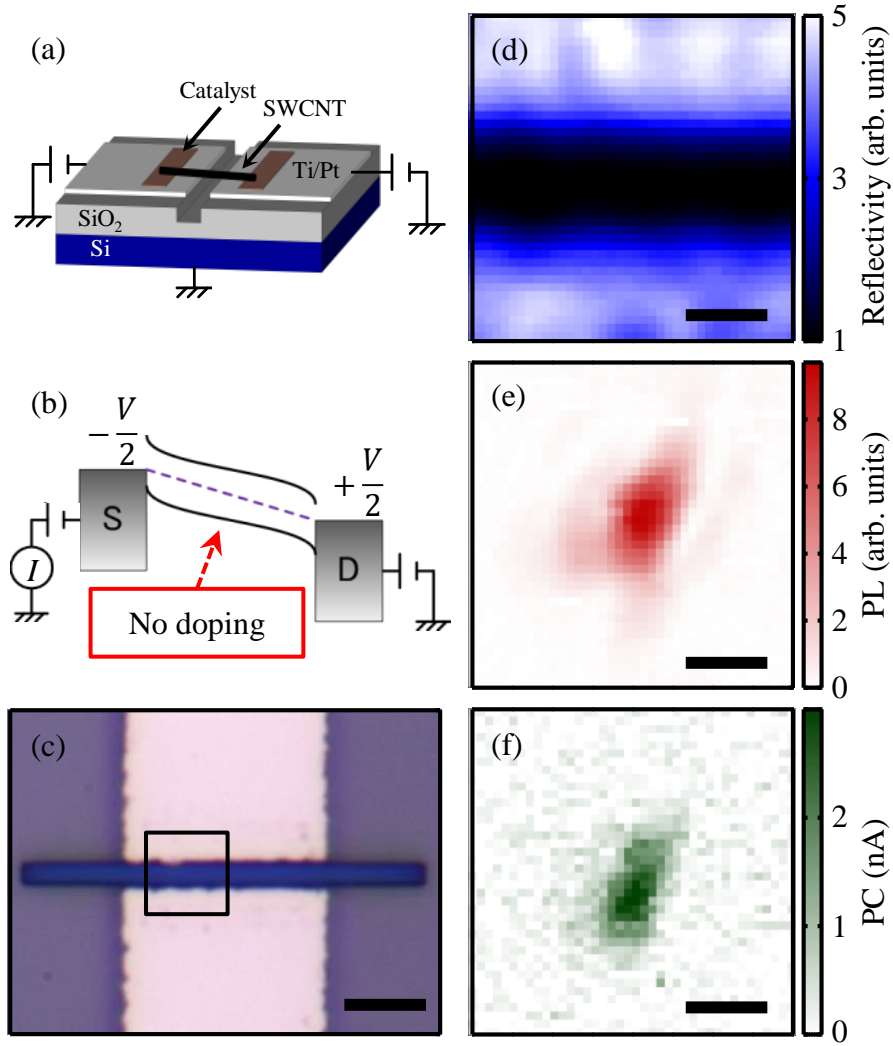


Figure 3.3: (a) A schematic of a device. (b) Energy-band diagram with symmetric bias voltages. (c) A top-view optical microscope image of a device with a trench width of $1.3 \mu\text{m}$. The black box shows the scan area for imaging measurements shown in (d)-(f). The scale bars in (b) and (c) are $0.5 \mu\text{m}$ and $4 \mu\text{m}$, respectively. (d), (e), and (f) are reflectivity, PL, and PC images, respectively. The scale bars are $1 \mu\text{m}$. Excitation energy and bias voltage are 1.651 eV and 20 V , respectively, and laser polarization angle is adjusted to maximize the PL signal. For (e), the PL image is extracted at an emission energy of 922 meV with a spectral integration window of 7 meV . Original data presented in Ref. [101].

3.1.4 Excitation spectroscopy

PL excitation spectroscopy performed on this nanotube at zero bias voltage shows a clear single peak [Fig. 3.4(a)], and we identify the nanotube chirality to be $(10, 6)$. By performing such an excitation spectroscopy under an application of bias, we obtain PL and PC excitation spectra simultaneously [Fig. 3.4(b)]. Both

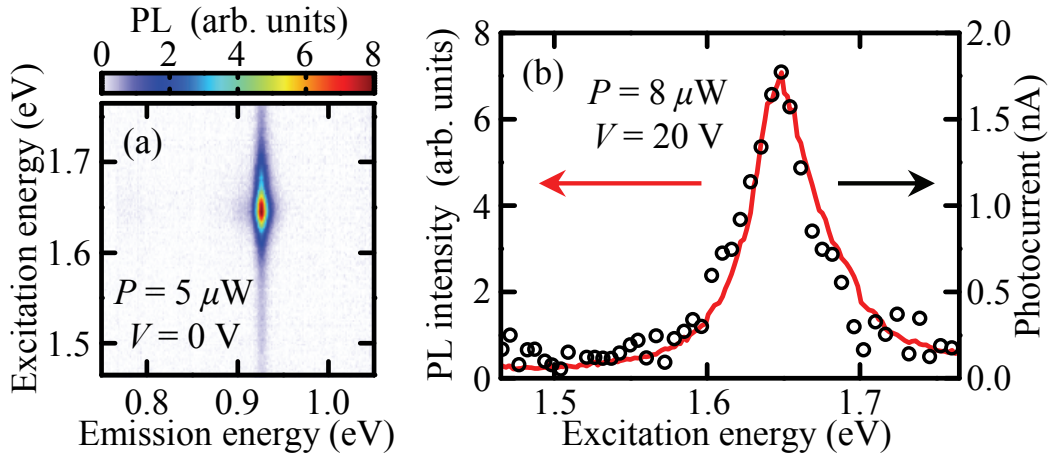


Figure 3.4: (a) A PL excitation map for the same nanotube as shown in Fig. 3.3(d-f) for $P = 5 \mu\text{W}$ and $V = 0 \text{ V}$. (b) PL (red curve) and PC (open circles) spectra taken with $P = 8 \mu\text{W}$ and $V = 20 \text{ V}$. Laser polarization is parallel to the nanotube axis. PL intensity is obtained by fitting the emission spectra with Lorentzian functions and taking the peak area. Original data presented in Ref. [101].

PL and PC have a peak at the same excitation energy corresponding to the E_{22} resonance. The spatial and spectral coincidence of the PL and PC signals show that both are indeed coming from the same nanotube.

3.2 Spontaneous exciton dissociation in carbon nanotubes

3.2.1 Exciton dissociation in nanotubes

Enhancement of the Coulomb interaction occurs in one dimensional systems because of limited screening [113], and single-walled carbon nanotubes (SWCNTs) are an ideal model system where such an effect manifests itself [13]. Electron-hole pairs form tightly-bound excitons with a binding energy of a few hundred meV, which amounts to a significant fraction of the band gap energy [14, 15]. Such a large binding energy warrants the stability of excitons even at room temperature, and with exciton size being a few nm [12, 114], strong fields on the order of $100 \text{ V}/\mu\text{m}$ would be required for exciton dissociation [59].

In contrast to the expectation that generation of free carriers from charge-neutral excitons would be difficult, photocurrent and photovoltaic measurements

have proved to be simple and convenient tools for studying the properties of SWCNTs. Not only have they been used to measure potential landscapes [82, 110–112], optical absorption properties [75, 115, 116], and ultrafast carrier dynamics [74], they have been instrumental in investigating unique effects that occur in SWCNTs, such as band-gap renormalization [117] and multiple electron-hole pair generation [70]. It has been a perplexing situation where exciton dissociation has not been brought up as an obstacle for performing these experiments. In interpreting the results, quantitative discussion on the dissociation process has been scarce, and in some cases the excitonic effects have not been considered at all.

Here we resolve such an inconsistency by performing simultaneous PL and PC measurements on individual SWCNTs. Non-zero photoconductivity is observed even at small fields, indicating that excitons are spontaneously dissociating. A simple model is constructed to consistently describe the excitation power and voltage dependences of the PL and PC. Using this model, we find that a good fraction, if not majority, of excitons are dissociating into free carriers. Within the same analysis framework, we are also able to extract the absorption cross section and the oscillator strength at the E_{22} resonance.

3.2.2 Excitation power and bias voltage dependences

On the device which is characterized in Sec. 3.1.3 and Sec. 3.1.4, the excitation power and bias voltage dependences are investigated in Fig. 3.5(a-d). We first discuss the excitation power dependence. For all of the voltages, the PC signal shows a linear increase with excitation power [Fig. 3.5(a)], whereas PL shows a sublinear increase [Fig. 3.5(b)]. The latter behavior is known to be caused by exciton-exciton annihilation [109, 118–120]. If the observed PC is caused by dissociation of the E_{11} excitons, then we expect PC to scale with PL, as both of the signals should be proportional to the number of E_{11} excitons.

Rather, the linear behavior suggests that the PC is proportional to the number of excitons injected at the E_{22} energy, and that dissociation of E_{11} excitons is negligible. There are at least two different processes that can result in the dis-

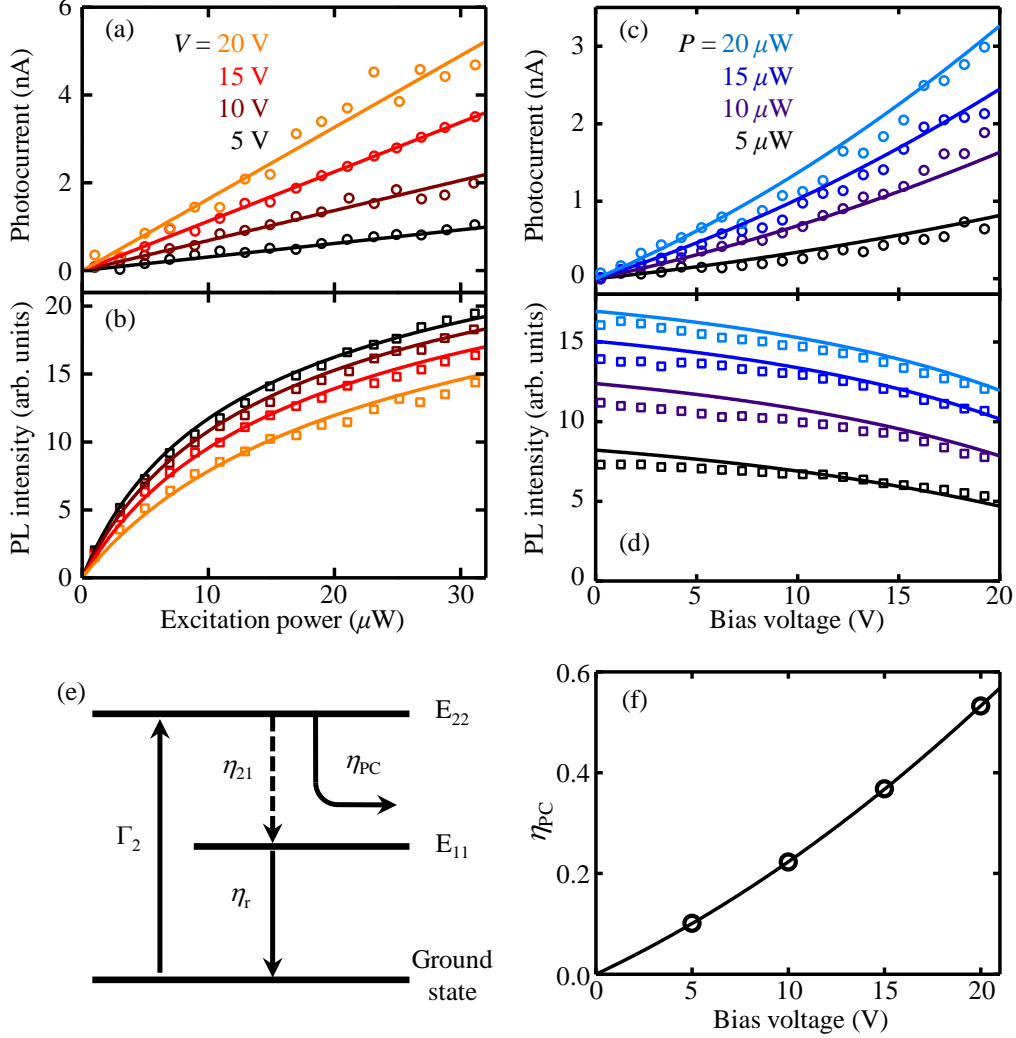


Figure 3.5: (a) Excitation power dependence of PC. Data from bottom to top correspond to $V = 5, 10, 15,$ and 20 V. (b) Power dependence of PL, with data from top to bottom corresponding to $V = 5, 10, 15,$ and 20 V. (c) and (d) Bias voltage dependence of PC and PL, respectively. Data from bottom to top correspond to $P = 5, 10, 15,$ and 20 μW . For (a-d), the same tube as shown in Fig. 3.3(d-f) was measured with the laser spot at the center of the nanotube. The excitation energy is fixed at 1.651 eV and the laser polarization is parallel to the nanotube axis. Symbols are data and lines are simulation results as explained in the text. (e) A schematic of the model used to produce the curves shown in (a-d). (f) η_{PC} as a function of V . Open circles are data obtained from (b) and the line is a fit as explained in the text. Original data presented in Ref. [101].

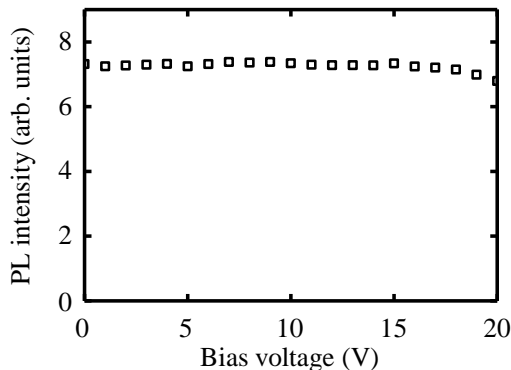


Figure 3.6: Bias voltage dependence of PL under E_{12} resonant excitation (1.476 eV). Data is taken with $P = 1000 \mu\text{W}$, and laser polarization is perpendicular to the nanotube axis. Original data presented in supplementary information of Ref. [101].

sociation of E_{22} excitons. It is possible that the applied electric field induces the dissociation, and in this case one would expect some threshold voltage at which the dissociation occurs [59]. Another conceivable scenario is the dissociation that happens spontaneously in the course of relaxation down to E_{11} exciton states.

The two pictures can be distinguished by examining the voltage dependence of the PC [Fig. 3.5(c)]. We observe that the PC has a slightly superlinear dependence on the applied voltage, but there exists some slope near $V = 0$. This implies that the conductivity is non-zero even at zero applied bias, supporting the interpretation that the injected excitons are spontaneously dissociating. Those carriers that are swept into the contacts before binding into E_{11} excitons would generate the PC.

We note that the lack of field-induced dissociation for E_{22} excitons is consistent with the interpretation of the intensity dependences that E_{11} exciton dissociation is negligible. The binding energy for E_{22} excitons is larger than E_{11} excitons [121], and therefore we do not expect field-induced dissociation of E_{22} excitons if E_{11} excitons are still intact. Measurements with excitation at the E_{12} resonance do not show much change in PL intensity with voltage [Fig. 3.6], also suggesting that field-induced dissociation is not important at these fields.

As the continuum for E_{11} exciton lies below E_{22} , it may seem reasonable to attribute the spontaneous dissociation to direct electronic transition to free

electron-hole pairs. It has been suggested, however, that such a process is much weaker than phonon mediated relaxation to E_{11} and E_{12} exciton states [122]. Since relaxation to excitonic states does not result in free carriers, we speculate that dissociation involving a free electron-hole pair with an emission of a phonon may be responsible for the observed photocurrent. Another possible mechanism is the free carrier generation from E_{11} exciton-exciton annihilation [33]. As the annihilation process is extremely efficient for air-suspended nanotubes [109, 120], it may explain the existence of free carriers. It is not clear why we do not observe trion emission as in the case of micelle-encapsulated nanotubes [33].

The voltage dependence of the PL [Fig. 3.5(d)] shows decrease of PL with increasing voltage. Different from the case where no PC flows [85], we expect that less excitons relax into E_{11} at higher voltages as photocarriers are extracted into the contacts. As the current gives the absolute rate of electron-hole pairs extracted from the nanotube, we can deduce the number of excitons removed from the system. By modeling such a fractioning in the exciton population, we are able to determine the number of injected excitons, and in turn the absorption cross section.

Figure 3.5(e) shows a schematic of our model. E_{22} excitons are generated at a rate

$$\Gamma_2 = \int n\sigma \frac{2P}{\pi r^2 E} \exp(-2\frac{x^2}{r^2}) dx = \sqrt{\frac{2}{\pi}} \frac{n}{r E} \sigma P, \quad (3.1)$$

where $n = 130 \text{ nm}^{-1}$ is the number of atoms per length, σ is the absorption cross section per carbon atom, $r = 492 \text{ nm}$ is the $1/e^2$ radius of the laser spot, and E is the laser photon energy. The fraction of the excitons that are extracted by PC is denoted by η_{PC} , while $\eta_{21} = 1 - \eta_{\text{PC}}$ represents the fraction that relax down to the E_{11} sublevel. The fraction of the E_{11} excitons that recombine radiatively and contribute to PL is represented by a non-linear function $\eta_r(\Gamma_1)$ which includes the effects of exciton-exciton annihilation. Here, $\Gamma_1 = \Gamma_2 \eta_{21}$ is the rate at which the E_{11} excitons are populated.

The absolute values of η_{21} can be obtained from the excitation power dependence of PL [Fig. 3.5(b)]. At $V = 0$, there are no PC and therefore $\eta_{\text{PC}} = 0$ and $\eta_{21} = 1$. When voltages are applied, Γ_1 decreases by a factor η_{21} . By scaling

the excitation power to match the dependence at $V = 0$, the values of η_{21} are obtained for the four voltages. We plot $\eta_{PC} = 1 - \eta_{21}$ in Fig. 3.5(f).

3.2.3 Absorption cross section and oscillator strength

Having obtained the explicit values of η_{PC} , we can now determine σ . Within our model, the PC is given by

$$I = e\eta_{PC}\Gamma_2 = \sqrt{\frac{2}{\pi}} \frac{e\eta_{PC}n}{rE} \sigma P, \quad (3.2)$$

where e is the electron charge, and the only unknown parameter is σ . We find that a value of $\sigma = 2.4 \times 10^{-17} \text{ cm}^2$ best matches the PC data in Fig. 3.5(a). This value is comparable to recent measurements of σ at the E_{22} resonance in micelle-encapsulated tubes [123] and on-substrate tubes [124].

In addition to σ , the oscillator strength f is obtained using its relation to integrated absorption cross section [125]. We fit the E_{22} resonance with a Lorentzian profile and obtain a linewidth of $\hbar\gamma = 44.5 \text{ meV}$ where \hbar is the Planck constant, and we use $f = \epsilon_0 m c \sigma \gamma / e^2$, where ϵ_0 is the vacuum permittivity, m is the electron mass, and c is the speed of light. We find $f = 0.015$ which is somewhat larger compared to (6,5) nanotubes [114].

To verify the validity of our model, we simulate the intensity and voltage dependences of PC and PL using the parameters obtained above. For the voltage dependence of η_{PC} , we fit the data in Fig. 3.5(f) with a linear term and a quadratic term. We use an analytic expression derived in Ref. [119] for the form of $\eta_r(\Gamma_1)$, with the parameters adjusted to fit our data. As shown as solid lines in Fig. 3.5(a-d), the model consistently explains all the data simultaneously.

The behavior of η_{PC} shows that a large fraction of the injected excitons are dissociating, reaching a value as high as $\eta_{PC} = 0.53$ at $V = 20 \text{ V}$. We expect PC to saturate above a certain voltage when all free carriers are extracted, but we do not see any signs of such saturation. This suggests that there are much more free carriers available even at the highest bias voltage we used, implying that the majority of the injected excitons are dissociating.

In order to check the reproducibility and to obtain σ for other chiralities,

Table 3.1: Absorption cross section and oscillator strength for the eight nanotubes measured. Lorentzian fits to PL excitation spectra at $V = 0$ V are used to obtain the E_{22} energy and full-width at half-maximum $\hbar\gamma$. Taken from Ref. [101].

Chirality	E_{22} (eV)	$\hbar\gamma$ (meV)	σ ($\times 10^{-17}$ cm 2)	f
(8,7)	1.724	66.6	2.1	0.020
(8,7)	1.712	58.4	2.6	0.022
(8,7)	1.717	71.3	1.7	0.017
(8,7)	1.725	69.1	2.5	0.025
(9,7)	1.593	44.2	9.5	0.060
(9,8)	1.555	50.5	7.1	0.052
(10,6)	1.652	44.5	2.4	0.015
(10,8)	1.452	51.5	1.3	0.009

we have performed similar measurements on other devices and the results are summarized in Table 3.1. For four tubes with a chirality of (8, 7), we find that f falls within $\pm 20\%$ and that the values are close to the theoretical estimate of $(0.014 \text{ eV}^{-1})E_{22} = 0.024$ [121]. We have observed that σ can differ by a factor of three or so for other chiralities, but additional measurements should be performed as these are based on single devices for each chirality.

We note that our model does not consider any direct recombination of E_{22} excitons which occurs prior to relaxation to the E_{11} state, for example exciton-exciton annihilation at the E_{22} level [126]. Such a process would lead to an underestimate of the number of injected excitons, and σ would be larger than what we have deduced from our model. We also do not take into account any field-induced changes to η_r , but further measurements at different excitation energies are expected to clarify the contribution of such effects.

3.3 Stark effect of excitons in individual air-suspended carbon nanotubes

3.3.1 Stark effect in nanotubes

Understanding of electric field effects on optical properties of single-walled carbon nanotubes (SWCNTs) is important for applications in nanoscale opto-

electronic devices [42]. One of the intriguing electro-optic effects is the Stark effect, which causes redshifts on exciton resonances under an application of electric fields [59,60]. The effect has been used to explain spectral changes in electroabsorption [63,65,66], photoconductivity [75], and ultrafast measurements [127]. Local variation of excitonic energies [128] and spectral diffusion at low temperatures [129,130] have also been attributed to the Stark effect. These experiments, however, have been performed on ensembles of nanotubes [63,65,66], without well-defined electric fields [127–130], or on nanotubes with unknown chirality [63,75], making quantitative analysis difficult.

Here we investigate field-induced redshifts of E_{11} exciton emission in chirality-assigned individual SWCNTs. Photoluminescence spectra of air-suspended nanotubes within field-effect transistor structures are collected under an application of symmetric bias voltages on source (S) and drain (D) contacts, revealing redshifts that scale quadratically with electric field. We find that the shifts do not depend much on excitation power or energy, ruling out effects from heating or relaxation pathways. Attributing the redshifts to the Stark effect, we have also performed measurements on different chiralities, and a reasonable agreement with theoretical predictions [59] is obtained by considering exciton binding energies for air-suspended tubes. Analysis using the total field rather than the longitudinal component shows more consistency, suggesting that transverse fields induce shifts of similar magnitude.

3.3.2 Electric field dependences of photoluminescence and current

Figure 3.7(b) shows PL spectra taken with longitudinal electric fields $F = 0$ and $15 \text{ V}/\mu\text{m}$ on the (10,6) nanotube used in the previous section under excitation at the E_{22} resonance and a power $P = 10 \mu\text{W}$. The emission peak with $F = 15 \text{ V}/\mu\text{m}$ shows a redshift as well as a reduction of intensity compared to $F = 0 \text{ V}/\mu\text{m}$. To investigate such a behavior in detail, we have measured the field dependence of PL spectra from 0 to $15 \text{ V}/\mu\text{m}$ [Fig. 3.7(c)]. The peak position,

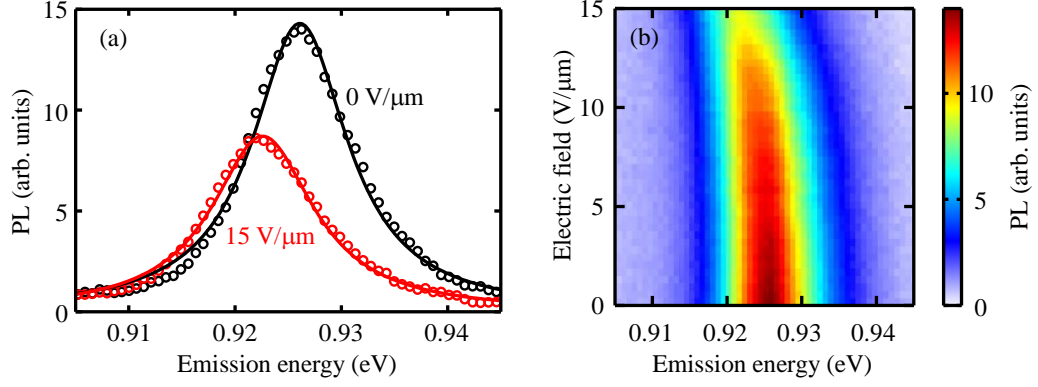


Figure 3.7: (a) A schematic of a device. (b) PL spectra taken with electric fields of $0 \text{ V}/\mu\text{m}$ (black) and $15 \text{ V}/\mu\text{m}$ (red). Open circles are data, and lines are Lorentzian fits. (c) PL spectra as a function of electric field. Data in (b-c) are taken with excitation energy of 1.651 eV and excitation power of $10 \mu\text{W}$, and a (10,6) tube with a suspended length of $1.3 \mu\text{m}$ characterized in Sec. 3.1.3 and Sec. 3.1.4 is used. Laser polarization is parallel to the nanotube axis. Original data presented in Ref. [102].

width, and area are extracted by fitting the spectra with a Lorentzian function, and we obtain good fits as shown in Fig. 3.7(b). Such fits have been performed for all of the spectra in Fig. 3.7(c) in order to quantitatively characterize the field dependence.

In Fig. 3.8, we plot the electric field dependence of emission energy, linewidth, peak area, and current. The PL peak area decreases with increasing field as photocarriers flow into the contacts [101]. We note that only those devices that show $\text{PC} > 0.3 \text{ nA}$ are investigated here, which is sufficiently larger than the noise level. If PC is small, it is likely that the nanotube has a bad contact to the electrodes, and the bias voltage can act as an effective gate. It is important to avoid such devices as unintentional electrostatic doping can occur, which is known to cause blueshifts [87].¹

¹We note that the voltage drop at the contacts should be negligible because the OFF state resistance of the nanotube (a few $\text{G}\Omega$) is larger than the contact resistance (a few $\text{M}\Omega$) or the metal pad resistance ($< 100 \Omega$) in our devices. Typical ON state resistance of 1-nm diameter nanotubes are $40 \text{ k}\Omega/\mu\text{m}$ and typical ON/OFF ratios range from 10^5 to 10^6 [131], and therefore the resistance of a few $\text{G}\Omega$ is reasonable for an OFF state resistance. Furthermore, our devices have shown a resistance of a few $\text{M}\Omega$ in the ON state for a similar diameter SWCNT [87]. As mentioned above, the ON state resistance of nanotubes is low, so in this case the contact

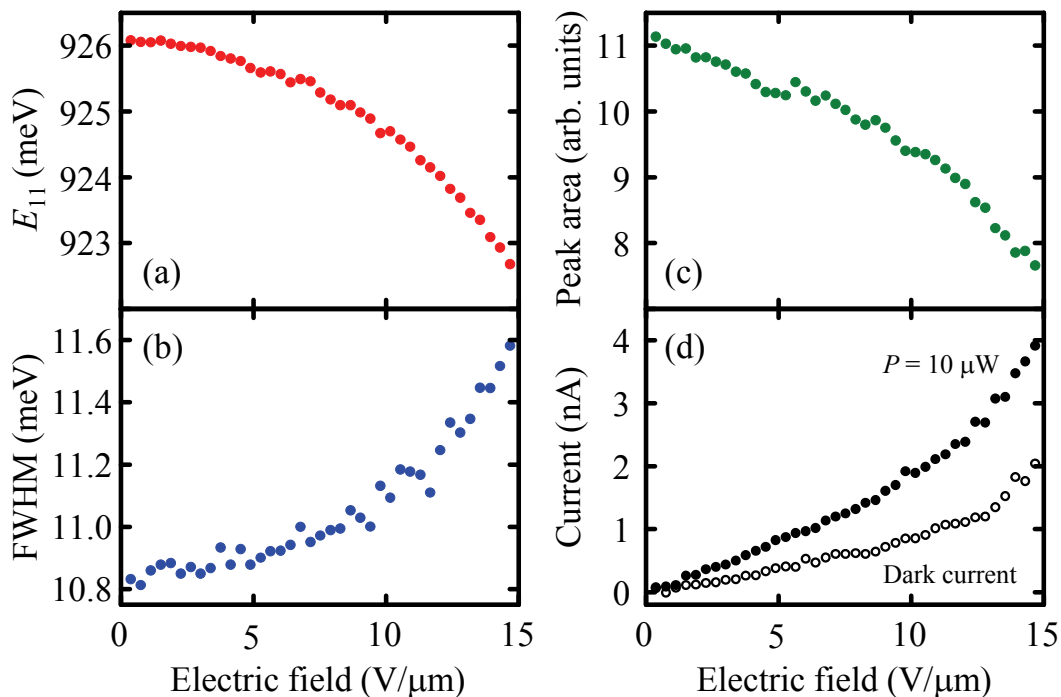


Figure 3.8: (a-c) Electric field dependence of emission energy, full width at half maximum (FWHM), and peak area, respectively, obtained from fits to data in Fig. 3.7(c). (d) Current taken with $P = 10 \mu\text{W}$ (filled circles) and the dark current (open circles) as a function of electric field. Original data presented in Ref. [102].

3.3.3 Redshifts induced by Stark effect and heating

The emission energy [Fig. 3.8(a)] shows a quadratic redshift on the electric field, as expected from the Stark effect [59]. The redshifts, however, could result from a rise in temperature [132] caused by Joule heating, as there exists a current flowing in the tube [Fig. 3.8(d)]. Such a heating effect can be quantified from the linewidth broadening [Fig. 3.8(b)]. In the case of $F = 15 \text{ V}/\mu\text{m}$, the tube temperature increase is estimated to be $\sim 32 \text{ K}$ by using a coefficient of 0.023 meV/K [133].

In order to identify the contribution of the heating-induced redshifts, we have investigated the excitation power dependence of the current, broadening, and redshift at different F [Fig. 3.9(a-c)]. Because the current increases with the excitation power [Fig. 3.9(a)], heating can be varied under fixed fields to isolate the temperature-induced redshifts. At $F = 15 \text{ V}/\mu\text{m}$, the broadening changes by

resistance likely dominates, giving an estimated contact resistance of the order of a few $\text{M}\Omega$.

a factor of 2.3 between $P = 5 \mu\text{W}$ and $25 \mu\text{W}$ [Fig. 3.9(b)], while the redshift only increases by 25% [Fig. 3.9(c)], showing that the thermal effects are limited. The data also indicate that 0.8-meV redshift occurs when heating causes 1-meV broadening, and using this relation, we estimate the heating-induced shift to be less than 22% of the redshift for the data taken at $P = 10 \mu\text{W}$ and $F = 15 \text{ V}/\mu\text{m}$. This is consistent with a redshift expected from the temperature dependence of emission energy [132] when the heating estimated from the linewidth broadening is used.²

We further consider whether the temperature increase of 32 K is reasonable by solving a heat conduction equation in one dimension with a fixed temperature at the ends³. A rise in the temperature by 2 K at the center of the tube is obtained for uniform Joule heating of $58 \text{ nW}/\mu\text{m}$ and assuming a thermal conductivity of $3600 \text{ W}/(\text{m K})$ [134]. A contact thermal resistance of $490 \text{ K m}/\text{W}$ can explain the remainder of the temperature increase for a contact length of $1 \mu\text{m}$, and this value is within the range observed for multi-walled nanotubes on Pt [135].

Measurements at different excitation energies have also been performed [Fig. 3.9(d)], and the electric-field dependence shows similar quadratic behaviors for excitation at the E_{12} , E_{11}^1 , and E_{11}^2 states [16]. These results show that relaxation pathways from the excited states to the E_{11} state do not influence the shifts of the emission energy, and that the redshifts are the intrinsic response of the E_{11} excitons under electric fields.

²Fig. 3.10 shows a correlation between redshift and broadening for different electric fields using data in Fig. 3.9(b-c). This plot indicates that the field-induced shift is dominant over heating-induced shifts. If heating is responsible for all of the redshift, all of the data points should collapse to a line that goes through the origin, regardless of the applied field. It is also clear that the redshift can be completely different depending on the electric field, even if the amount of heating is the same (e.g., redshift at the four different fields can be compared at a broadening of 0.6 meV).

³See Appendix B.

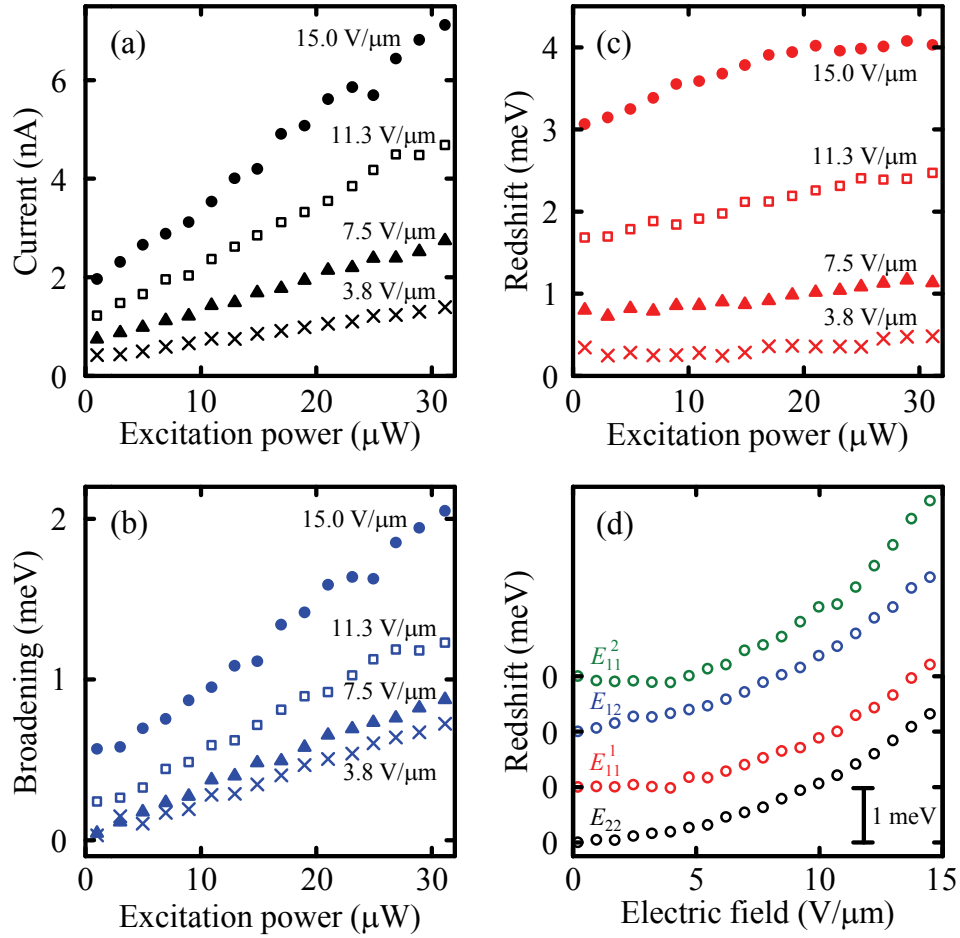


Figure 3.9: (a-c) Excitation power dependence of current, broadening, and redshift, respectively. Data from bottom to top correspond to $F = 3.8, 7.5, 11.3,$ and 15.0 V/ μm . The excitation energy is fixed at 1.651 eV. The tube is the same as in Fig. 3.7 and Fig. 3.8. The broadening and redshift are measured from 10.7 meV and 926.3 meV, respectively, taken at $P = 1$ μW and $F = 0$ V/ μm . (d) Field-induced redshift as a function of F taken at different excitation energies. Data from bottom to top are taken at E_{22} (1.651 eV), E_{11}^1 (1.351 eV), E_{12} (1.476 eV), and E_{11}^2 (1.450 eV) resonances [16], where $P = 5, 150, 1000,$ and 200 μW are used, respectively. The data are offset for clarity. The laser polarization is parallel to the tube except for E_{12} excitation in (d) where it is perpendicular. Original data presented in Ref. [102].

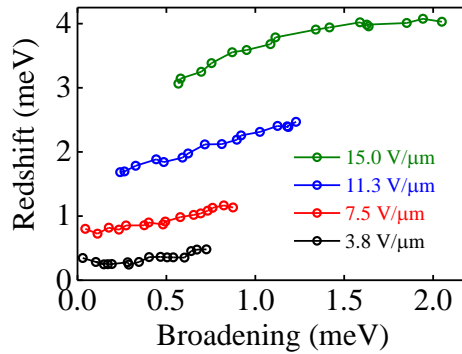


Figure 3.10: Redshift as a function of broadening for different electric fields.

3.3.4 Chirality dependence

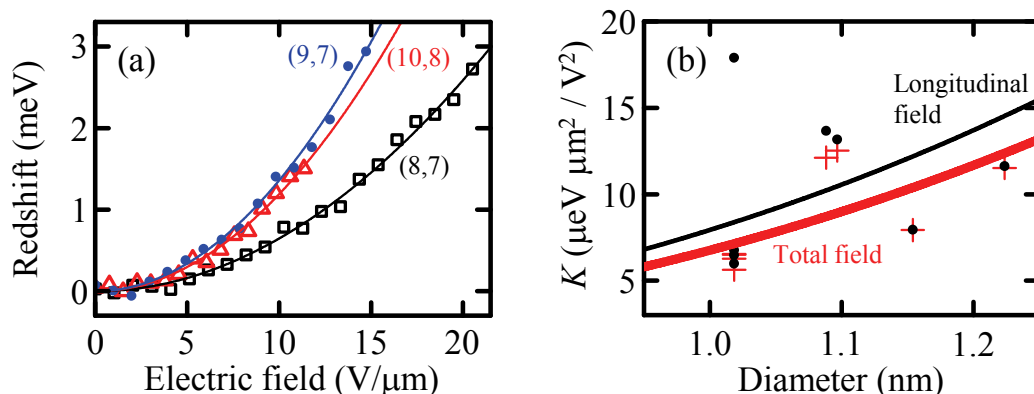


Figure 3.11: (a) Stark effect for a 1.0- μm -long (8,7) tube (squares), a 1.3- μm -long (10,8) tube (triangles), and a 1.0- μm -long (9,7) tube (dots), measured with E_{22} excitations. For the (8,7), (10,8), and (9,7) tubes, $P = 8, 10,$ and $5 \mu\text{W}$ are used, and the redshifts are measured from 998.5, 862.7, and 954.7 meV, respectively. (b) Diameter dependence of K . Dots and crosses show data analyzed with longitudinal field and total field, respectively. Lines are fits. Original data presented in Ref. [102].

We therefore attribute the redshift to the Stark effect, and nanotubes with different chiralities have also been investigated (Fig. 3.11). The measurements are performed with the laser polarization parallel to the tubes, and at low powers such that the field-induced linewidth broadening is 0.6 meV or less. All of the tubes show redshifts that increase quadratically with electric fields, but the amounts of the shifts are different [Fig. 3.11(a)]. In order to characterize the strength of the effect, the data are fit to

$$\delta E_{11} = KF^2, \quad (3.3)$$

where δE_{11} is the redshift and K is a constant. The values of K obtained for the eight tubes measured are plotted as a function of the tube diameter d [dots in Fig. 3.11(b)]. The diameter dependence of the Stark effect is expected to be [59]

$$K = \kappa_b \frac{(ed)^2}{E_b}, \quad (3.4)$$

where κ_b is a unitless constant, e is the electronic charge, and $E_b = 0.66/d$ eV is the exciton binding energy for air-suspended nanotubes [16]. The thin line in Fig. 3.11(b) shows the fit to the data using Eq. 3.4. We obtain $\kappa_b = 5.2$, which is

comparable to the theoretical values ranging from 3.0 to 4.2 in Ref. 59, although the data has a large scatter.

In particular, of the four (8,7) nanotubes we have measured, one shows a relatively large K . It turns out that this nanotube is suspended at an angle of 37° with respect to the trench. Since the electric field is established between the source and drain contacts, this tube is at a large angle with the field. If transverse fields can also induce Stark shifts [63, 75], it may explain the deviation as the analysis so far only considered the longitudinal component.

When we replot the data using the total field [crosses in Fig. 3.11(b)] as opposed to the longitudinal field, we find that K of the four (8,7) tubes falls within $\pm 9\%$. In addition, $\kappa_b = 4.5$ is obtained [thick line in Fig. 3.11(b)], which is closer to the theoretical values. Although the data still show some deviations from Eq. 3.4, our results are in reasonable agreement as the calculations also find chirality dependent κ_b that can differ by $\pm 17\%$.

With the reasonable agreement with theory, we can estimate the exciton dissociation time under the experimental conditions. The dissociation rate can be written as [59]

$$\Gamma = \alpha E_b \frac{F_0}{F} \exp\left(-\frac{F_0}{F}\right), \quad (3.5)$$

where $\alpha = 4.1$ is a constant and F_0 is the dissociation field. For a $d = 1.1$ nm tube with $E_b = 288$ meV, F_0 has been calculated to be 198 V/ μm in Ref. 59. Using the relation $F_0 \propto E_b^{3/2}$, we estimate $F_0 = 595$ V/ μm for an air-suspended (10,6) tube by scaling for $E_b = 600$ meV. The dissociation time \hbar/Γ , where \hbar is the Planck constant, is longer than 1 s for the highest applied field of 15 V/ μm , and as the lifetime of E_{11} excitons is much less than 1 ns [120], we do not expect E_{11} exciton dissociation at these fields [101].

3.4 Conclusions

We have performed simultaneous PL and PC spectroscopy on individual air-suspended SWCNTs and constructed a model that consistently explains the excitation power and voltage dependences. Within the voltage range explored, we did

not find evidences of field-induced exciton dissociation, for either of the E_{11} and E_{22} excitons. Instead, a considerable fraction of the injected excitons are found to spontaneously dissociate into free electron-hole pairs. We have also obtained the absorption cross section and the oscillator strength from these air-suspended SWCNTs. Our findings explain why the large exciton binding energies do not impede photoconductivity measurements in SWCNTs.

In addition, we have investigated the redshifts of PL emission from SWCNTs caused by electric fields. Since the shifts are quadratic in field and not dependent on excitation power or energy, they are attributed to the Stark effect. By performing measurements on different chiralities, we have shown that the shifts are in quantitative agreement with theoretical calculations. The results on tubes at large angles with the field suggest that transverse fields may be causing Stark shifts of similar magnitude. As the estimated dissociation rates are negligible, it should be possible to achieve wider control of emission wavelength in stronger fields or larger diameter tubes.

Chapter 4

Gate-voltage induced trions in suspended carbon nanotubes

In Chapter 3, we described how bias voltages affect excitons in carbon nanotubes, and we have observed spontaneous exciton dissociation and the Stark effect of excitons. Using the FET structures, we are also able to investigate gate voltage effects on excitons as well as the bias effects. In this chapter, we therefore have performed PL measurements under an application of gate voltages, and have observed trion (charged exciton) emission from suspended carbon nanotubes where carriers are introduced electrostatically.

4.1 Trions in nanotubes

The quasi-one-dimensional geometry of single-walled carbon nanotubes results in enhanced Coulombic effects that are sensitive to environmental dielectric screening. The strong electron-hole attractive force generates tightly bound excitons, but their binding energies can differ by a few hundred meV for surfactant-wrapped nanotubes compared to suspended nanotubes [16, 136]. Also because of the limited screening, a charged carrier can be bound to an exciton to form a trion that is stable even at room temperature [32, 33]. Such tightly bound trions have also been observed in atomically-thin two dimensional semiconductors such as transition metal dichalcogenide monolayers [38, 137]. Trions provide additional degrees of freedom for manipulating the optical properties of SWCNTs as

they possess both charge and spin, and consequently they have received considerable attention. Various techniques including photoluminescence (PL) [92, 138, 139], electroluminescence [140], absorption [91], and time-resolved [141–143] spectroscopy have been used to investigate trions, and it has been shown that trion generation in micelle-wrapped SWCNTs involves trapped charges [33, 138, 143]. Similar to the case of excitons, significantly enhanced trion binding energies are expected in suspended SWCNTs [29, 34, 35], but it has been pointed out that trion formation is difficult due to low exciton-carrier scattering rates [144].

Here we report on gate-voltage induced trions in suspended carbon nanotubes within field-effect transistor structures. When a gate voltage is applied, a peak emerges at an energy below the E_{11} bright exciton emission. Excitation spectroscopy under the application of the gate voltage shows that the absorption resonances for both the emission peaks are the same, indicating that they arise from the same nanotube. Gate-voltage dependence measurements reveal that bright exciton quenching and the appearance of the lower energy peak occur at the same voltage, consistent with the picture that electrostatic doping leads to trion formation. This interpretation is further confirmed by the observation that the energy separation between the bright exciton peak and the gate-induced peak becomes smaller for larger diameter tubes. We obtain trion binding energies that are considerably larger compared to surfactant-wrapped tubes, as expected from the dielectric screening effects.

4.2 Photoluminescence measurement system

PL measurements are performed with a home-built laser-scanning confocal microscope system (Figs. 4.1 and 4.2) [4, 109, 145–147]. We utilize a path switching mirror in order to use two sample stages in a single optical system. One of the stages is a motorized three-dimensional translation stage (Sigma tech, FC-401 and FS-1020X) with a travel length of $\pm 10000 \mu\text{m}$ in the sample plane [147], while the other is a custom-designed cryostat (Janis, ST-500) [4] which allows for PL measurements in vacuum for reducing gate hysteresis [108, 148]. We note

that the position of the cryostat on an XYZ linear stage (Newport, M-562-XYZ-LH) is determined by a micrometer (Newport, HR-13) and two actuators (Zaber, T-NA08A25) for the direction perpendicular and parallel to the optical table, respectively.¹

For excitation, a continuous-wave Ti:sapphire laser with a wavelength range from 700 to 950 nm is focused onto the sample by an objective lens for each sample stage.² Emission from the samples is focused into a 300-mm spectrometer by a 50-mm focal-length lens, and the PL is dispersed using a 150 lines/mm grating blazed at 1.25 μm . PL spectra are detected by an InGaAs photodiode array with a detection wavelength from 800 to 1700 nm (Princeton Instruments, OMA-V 1.7), or an extended range InGaAs photodiode array which can detect emission between 1000 and 2200 nm (Princeton Instruments, OMA-V 2.2) at the cost of a reduced signal-to-noise ratio (Table 4.1³).⁴ All measurements are done at room temperature.

Table 4.1: Specifications of linear InGaAs photodiode array (OMA-V 1.7 and 2.2).

	OMA-V:512-1.7	OMA-V:1024-2.2
Array size	500 μm \times 50 μm	500 μm \times 25 μm
Pixel	512 \times 1	1024 \times 1
Spectral range	0.8-1.7 μm	1.0-2.2 μm
Peak quantum efficiency	>80% @ 1.0-1.6 μm	>70% @ 1.4-2.0 μm
Dark signal	15 $\text{ke}^-/\text{p/s}$	1.5 $\text{Me}^-/\text{p/s}$

¹When the cryostat is used, it is difficult to perform the sample movement exactly because the accuracy of the Zaber actuators is 15 μm in spite of the 1- μm laser spot size. The position of the cryostat is therefore roughly determined by moving the XYZ stage, and then the laser spot is moved by a fast steering mirror (Optics in Motion, OIM-101).

²For the objective lens for the motorized 3D stage, an LMPlan IR \times 100 (OLYMPUS) is used. For the lens for the cryostat, we use an LCPLN50 \times IR (OLYMPUS) with a correction collar.

³ $\text{e}^-/\text{p/s}$: electrons/pixel/second

⁴We use a 50- μm pinhole for the OMA-V 1.7 and a 100- μm pinhole for the OMA-V 2.2.

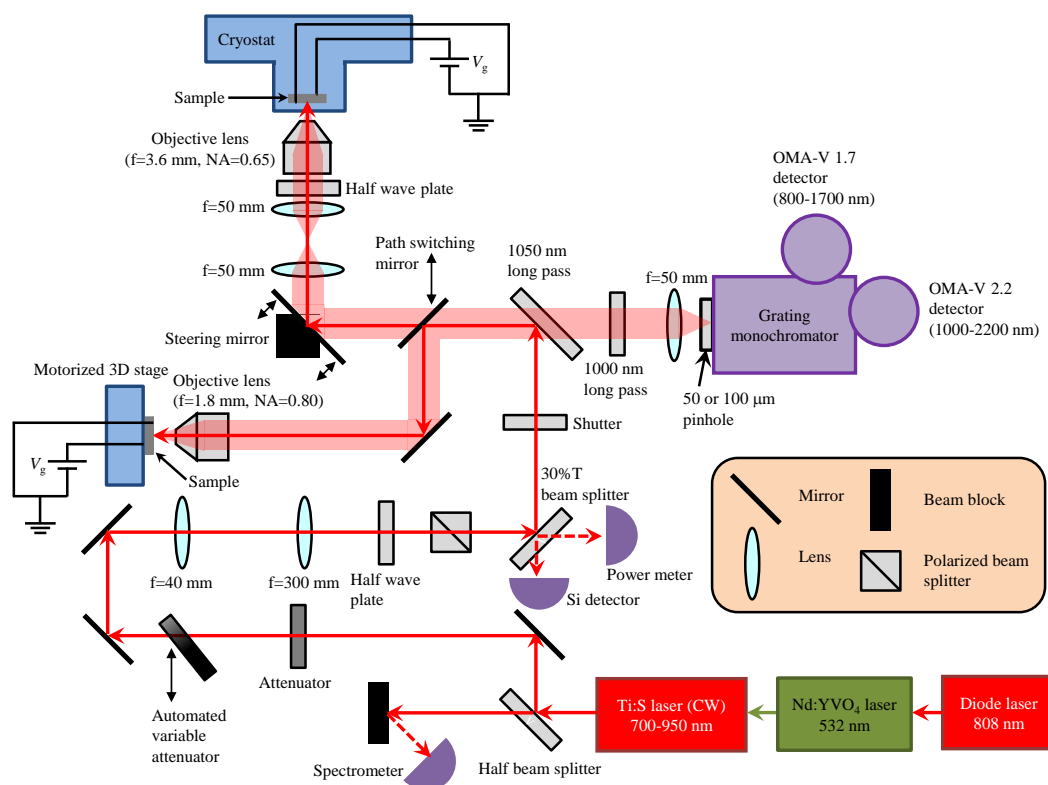


Figure 4.1: Schematic of photoluminescence measurement system.

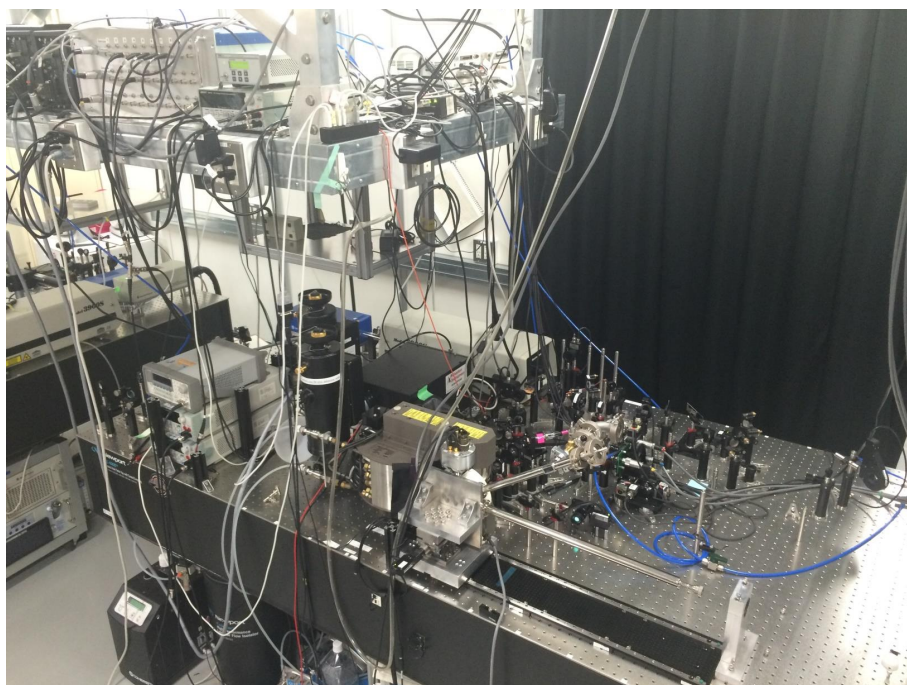


Figure 4.2: Photoluminescence measurement system in our optics lab.

4.3 Photoluminescence line scan measurements

In order to find suspended SWCNTs efficiently, we carry out PL line scan measurements along the trenches [99, 147] in type B devices (see Chap. 2). The samples are mounted on the motorized 3D stage as described in the previous section, and the measurements are done in air. Data are typically taken with an excitation power of $100 \mu\text{W}$, and laser polarization is perpendicular to the trenches. Trench scans are repeated 1-3 times using different excitation wavelengths to find SWCNTs with desired chiralities. From the scan results, we select nanotubes which show bright emission and then perform PLE spectroscopy with an excitation power of $5 \mu\text{W}$ for each of the nanotubes to determine their chirality. We exclude nanotubes with broad spectra or multiple strong peaks in the PLE, because such tubes may be bundled or other tubes may be present in the vicinity.⁵

After finding bright SWCNTs, PL spectra are taken with the back gate voltages $V_g = \pm 2$ or 5 V. If the nanotubes do not show PL quenching, they may not be suspended over the trenches or not be well contacted to the electrodes. In this case, we do not measure these tubes in the later sections.

4.4 Photoluminescence excitation spectroscopy with and without gate voltages

After such careful characterization, the samples are placed in the cryostat, and the chamber is pumped down to the 10^{-6} mbar range using a turbo molecular pump (Pfeiffer, TSH071E). We then close the valve of the cryostat, and stop the pump to eliminate vibration.

We perform PLE spectroscopy on the suspended nanotubes again since the E_{11} and E_{22} energies often change due to environmental effects [47, 49]. Typical data taken with an excitation power $P = 5 \mu\text{W}$ is shown in Fig. 4.3(a), where the tube chirality (n, m) is identified to be (10,5) by utilizing an empirical

⁵However, it seems that we could not exclude some of the bundled tubes as shown in Sec. 4.6.2.

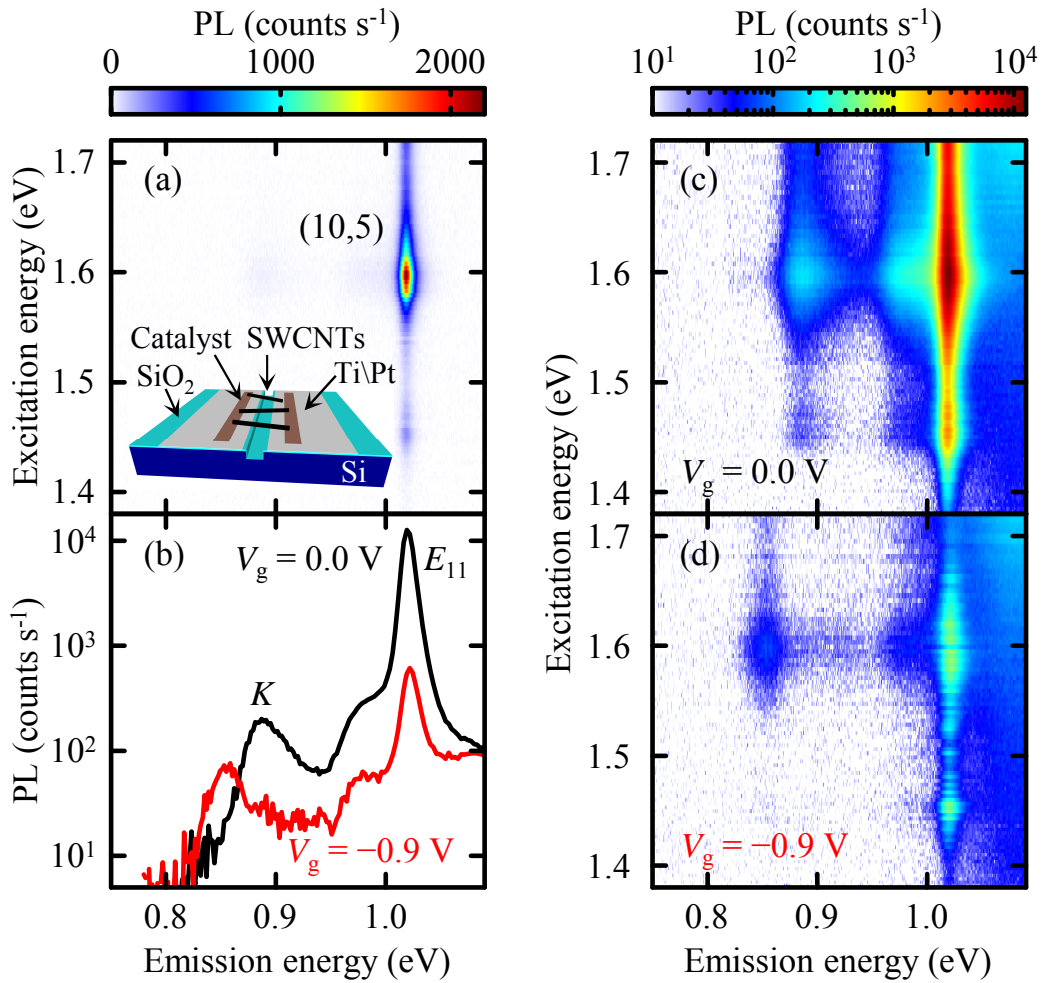


Figure 4.3: (a) A PLE map of an individual nanotube in a device taken with $P = 5 \mu\text{W}$. The absorption peaks at 1.60 and 1.45 eV correspond to the E_{22} and E_{11}^1 resonances, respectively [16]. The inset is a device schematic. (b) PL spectra taken at $V_g = 0.0 \text{ V}$ (black) and $V_g = -0.9 \text{ V}$ (red). An excitation energy of 1.60 eV is used. (c) and (d) PLE maps at $V_g = 0.0 \text{ V}$ and $V_g = -0.9 \text{ V}$, respectively. For (b-d), the excitation power is fixed at $P = 300 \mu\text{W}$, and the laser polarization is parallel to the nanotube axis. Weak emission above 1.0 eV comes from Si. Original data presented in Ref. [103].

table [99]. We verify that the nanotube is fully suspended over the trench by taking PL and reflectivity images, and the laser polarization dependence of PL is used to check that the nanotube is relatively straight [109]. After such careful characterization, we have investigated the effects of the voltage V_g applied to the back gate while grounding the nanotube contacts. Although PL is collected from the full suspended length of the tube, most of the emission originates from the center [99, 109] where the gate fields are expected to be more homogeneous. At

$V_g = 0.0$ V [Fig. 4.3(b), black curve], the E_{11} bright exciton peak is visible as well as a side peak at a lower energy, which is the K -momentum dark exciton state [27]. For the case of $V_g = -0.9$ V [Fig. 4.3(b), red curve], E_{11} and K -momentum exciton peaks show quenching as a result of electrostatic doping [87], and a new redshifted peak with 168-meV energy separation from E_{11} is observed. To rule out the presence of another tube in the vicinity, we have performed PLE spectroscopy at $V_g = 0.0$ [Fig. 4.3(c)] and -0.9 V [Fig. 4.3(d)]. We find that the E_{11} peak and the new peak exhibit similar absorption behaviors, confirming that the gate-induced peak originates from the same nanotube.

4.5 Gate voltage dependence of photoluminescence

In order to characterize the gate-induced peak in detail, gate voltage dependence of PL on this nanotube has been investigated [Fig. 4.4(a)]. By performing fits to these spectra by a Lorentzian function with a linear background, we have extracted the peak areas and emission energies for the E_{11} bright exciton, the K -momentum exciton, and the gate-induced peaks. In Fig. 4.4(b), the gate-voltage dependence of the spectrally integrated PL intensities of the peaks is shown, where the E_{11} emission quenches exponentially with V_g as observed previously [87]. In contrast, the new peak emerges with an application of gate voltage, and becomes maximized at $V_g = -0.9$ and 0.7 V. Such a behavior indicates that electrostatic carrier doping gives rise to the new peak, and we therefore assign the gate-induced peak to trion emission.

We estimate the carrier density at maximum trion intensity to be 0.014 nm^{-1} by modeling the device [87]. In comparison, typical chemical doping concentrations used to observe trion emission [32] correspond to about an order of magnitude higher hole densities [149]. We also find that the trion peak behaves symmetrically for positive and negative gate voltages. This results from effective masses of electrons and holes being almost the same, and have also been observed in previous work utilizing electrochemical [91, 92] and electrolyte gat-

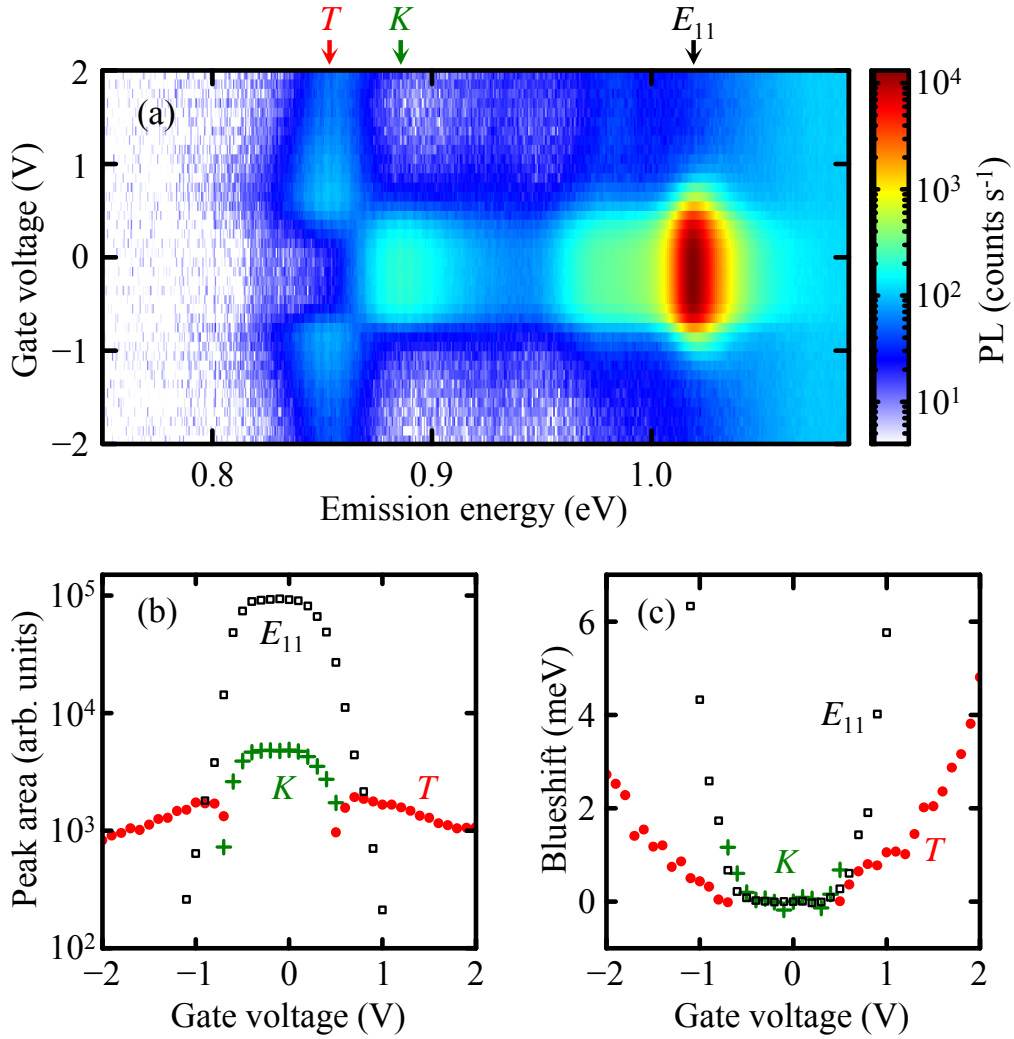


Figure 4.4: (a) PL spectra as a function of gate voltage taken at a sweep rate of 40 mV s⁻¹. The excitation energy is 1.60 eV and $P = 300 \mu\text{W}$ is used. The laser polarization is parallel to the nanotube axis. (b) and (c) Gate voltage dependence of peak area and blueshift, respectively, for E_{11} bright exciton (black squares, E_{11}), K -momentum dark exciton (green crosses, K), and gate-induced peaks (red dots, T). Fitting is done by a Lorentzian plus a linear function. For (c), the blueshifts are measured from 1020.4, 888.8, and 853.4 meV for the E_{11} exciton, K -momentum exciton, and gate-induced peaks, respectively. Original data presented in Ref. [103].

ing [140] techniques.

As the gate voltage increases further, the intensity of the trion peak gradually decreases [Fig. 4.4(b)], which may be caused by a reduction of E_{22} absorption cross section or changes in Auger recombination rates. In addition, the emission energies for all of the peaks show slight blueshifts with increasing gate voltage [Fig. 4.4(c)]. Such gate-induced energy shifts for bright exciton and trion peaks

have been observed previously [55,87,140], and may be caused by a combination of band-gap renormalization, band filling, and changes in the binding energies [62]. We note that the blueshift of the trion peak is smaller compared to the E_{11} peak, which may be caused by an increase of the singlet-triplet exciton splitting [32,33,92]. If the Stark effect of trions is larger than that for excitons [102], it may also explain the difference.

4.6 Nanotube diameter dependence

4.6.1 Individual nanotubes

Now we investigate the diameter dependence in order to determine the trion binding energy in suspended nanotubes. In Figs. 4.5(a-c), we present PL spectra taken with and without gate voltages on three nanotubes of different chiralities. All of the nanotubes show the emergence of the trion peak as well as quenching of the E_{11} and K -momentum exciton peaks upon application of gate voltages. Furthermore, the energy separation ΔE between the E_{11} peaks and the trion peaks decreases as the tube diameter becomes larger.

Such measurements are systematically performed on 100 individual nanotubes to obtain the nanotube diameter dependence of ΔE [blue circles and red dots in Fig. 4.5(d)]. We note that ΔE has been measured at a gate voltage where the E_{11} intensity has quenched by a factor of 10 to 100, such that both E_{11} and trion peak positions can be accurately determined. A clear diameter dependence as well as family patterns are observed, similar to the diameter dependence of trions in surfactant-wrapped SWCNTs [32,33,92]. In comparison, the K -momentum exciton peaks [green crosses in Fig. 4.5(d)] do not show such a dependence [27].

The diameter dependence of ΔE can be used to extract the trion binding energy. As the trion emission originates from a bound state of a triplet exciton and a charged carrier, the E_{11} -trion splitting is given by $\Delta E = A/d + B/d^2$, where the first term represents the trion binding energy and the second term is the singlet-triplet splitting [32,33,92]. Using $B = 70 \text{ meV}\cdot\text{nm}^2$ for suspended nanotubes [27], we obtain $A = 105 \text{ meV}\cdot\text{nm}$ by fitting the data [orange line in Fig. 4.5(d)].

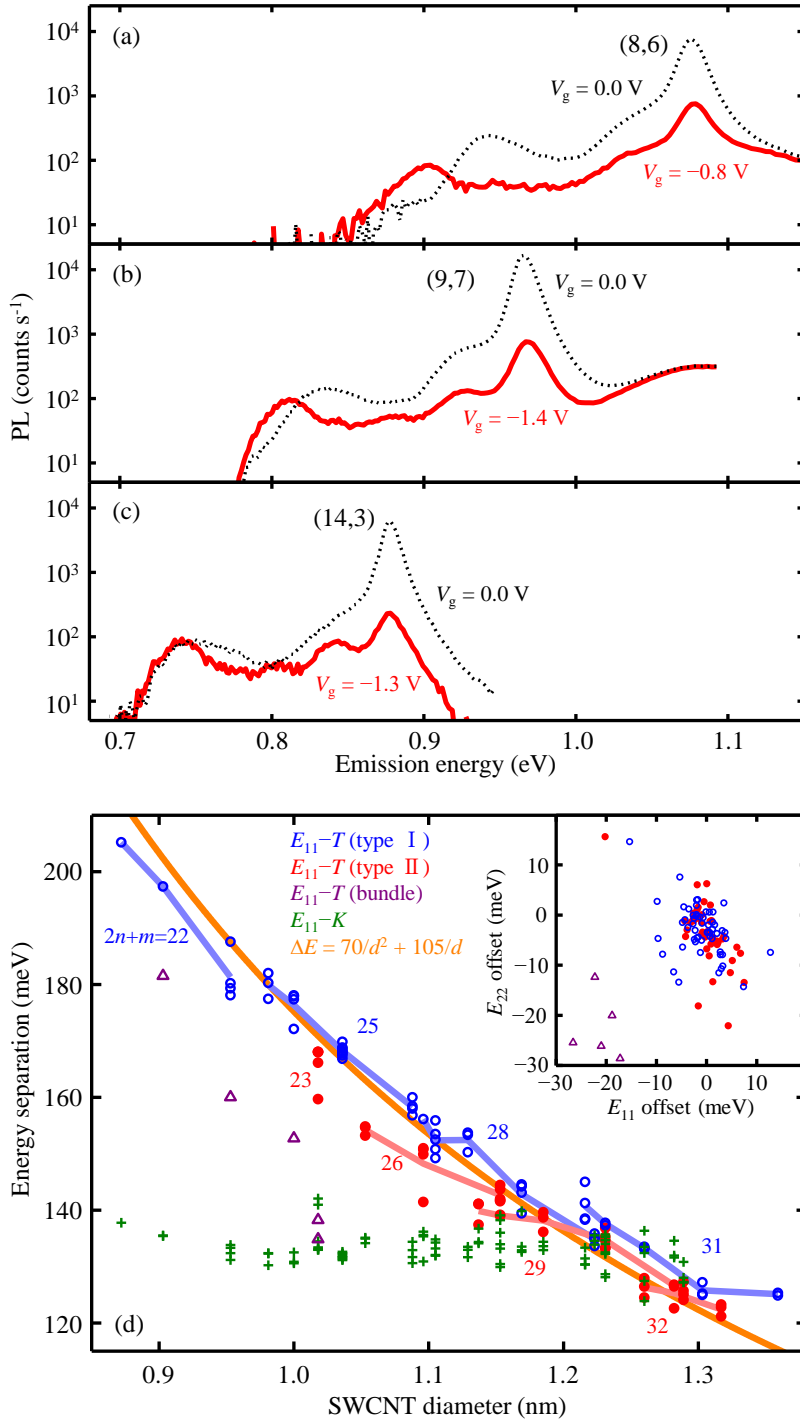


Figure 4.5: (a-c) PL spectra for (8,6), (9,7), and (14,3) nanotubes, respectively. Data are taken at zero gate voltage (black broken lines) and under an application of gate voltages (red solid lines). (d) Nanotube diameter dependence of energy separation ΔE between E_{11} and the trion peaks on 100 individual SWCNTs. Blue circles and red dots correspond to type I and type II nanotubes, respectively. Purple triangles show ΔE for bundled tubes. Green crosses indicate data on energy splitting between E_{11} and K -momentum exciton peaks. An orange line is a fit, while blue and red lines show the family patterns. All of the data are taken at E_{22} excitation and $P = 300 \mu\text{W}$. Laser polarization is parallel to each nanotube axis. Inset shows E_{11} and E_{22} energy offsets from tabulated PLE data in Ref. [99]. Original data presented in Ref. [103].

The value is significantly larger than the binding energy in surfactant-wrapped SWCNTs which ranges from 49 to 85 meV·nm [32, 33, 92], and the difference is likely caused by dielectric screening from the surrounding ambient [29, 34, 35]. As the exciton binding energy in SWCNTs increases by a factor of 1.5 for suspended tubes compared to surfactant-wrapped tubes [16], the extracted value of A is fairly reasonable since the power-law scaling of exciton and trion binding energies with respect to dielectric constant is similar [29, 121].

4.6.2 Bundled nanotubes

We note that 5 suspended SWCNTs [triangles in Fig. 4.5(d)] display ΔE that is lower by about 30 meV from the fit. For these tubes, both E_{11} and E_{22} energies are significantly redshifted compared to tabulated PLE data in Ref. [99] as shown in Fig. 4.5(d) inset. The redshifted peaks forming satellite spots in the PLE map have been interpreted as bundles of nanotubes with the same chirality [99], in which the increased screening reduces the optical transition energies with respect to individual SWCNTs. The smaller E_{11} -trion energy splitting is consistent with this interpretation. In Fig. 4.6, we present an example of PLE maps and PL spectra for individual and bundled (8,6) SWCNTs.

4.7 Conclusions and outlook

We have investigated gate-induced trion emission in suspended carbon nanotubes with assigned chirality. Gate voltage dependence of PL shows coincidence of bright exciton quenching and gate-induced peak emergence, indicating that trions are generated by electrostatic doping. By performing measurements on tubes with different chiralities, we confirm that the E_{11} -trion energy splitting becomes smaller with increasing tube diameter. The trion binding energies are found to be significantly larger than those in surfactant-wrapped SWCNTs, which can be explained by dielectric constant scaling of the binding energies.

The observation of trions in electrostatically-doped clean SWCNTs opens up new prospects for spin manipulation. The trions in suspended nanotubes may

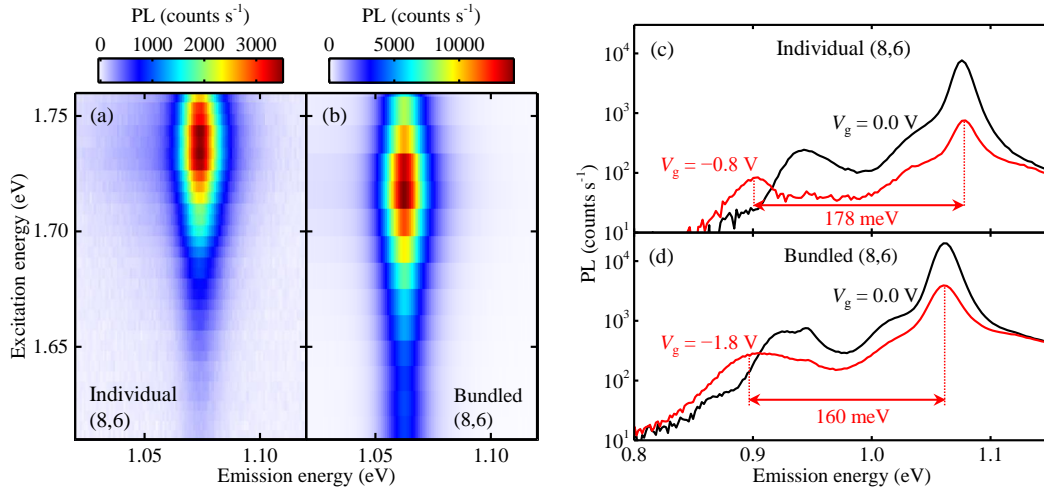


Figure 4.6: (a-b) PLE maps for individual and bundled (8,6) nanotubes, respectively. Excitation power is $10 \mu\text{W}$ for (a) and $50 \mu\text{W}$ for (b). For (a), E_{11} and E_{22} energies show redshifts of 5.5 meV and 13.4 meV compared to (8,6) PLE data in Ref. [99], respectively. For (b), we observe 17.2-meV E_{11} redshift and 28.6-meV E_{22} redshift from the data in Ref. [99] (c-d) PL spectra for individual and bundled (8,6), respectively. Data are taken with zero gate voltage (black) and under an application of gate voltages (red). Laser power is $300 \mu\text{W}$, and laser polarization is parallel to the tube axes. ΔE of the bundled tube is smaller than that of the individual tube.

be delocalized, in which case they would allow for spin transport along the tube. As trions are charged particles, it should be possible to drive them by applying longitudinal electric fields. There may be new opportunities for investigating spin properties in nanotubes by utilizing trion emission for detection.

Chapter 5

Conclusions

We have investigated electric field effects on excitons in individual chirality-assigned suspended carbon nanotubes within field effect transistor structures. By performing photoluminescence and photocurrent measurements under electric fields, three types of phenomena in nanotubes have been elucidated, which are spontaneous exciton dissociation, Stark effect of excitons, and gate-voltage induced trions.

Through simultaneous photoluminescence and photocurrent measurements with an application of symmetric bias voltages, we have observed nonzero photoconductivity at small fields, suggesting that excitons are spontaneously dissociating. Considering required fields for dissociation of E_{11} exciton with a large binding energy, our results seem to be counterintuitive, but free carrier generation may be happening during the path of relaxation from excited states to E_{11} exciton states or through exciton-exciton annihilation. Although the exciton dissociation mechanism is still unclear, our results provide a hint for understanding fundamental physics underlying photocurrent generation in nanotubes, which is a key to nanoscale device applications such as photodiodes and solar cells.

We have also observed quadratic PL redshifts on electric fields, which is caused by Stark effect of excitons. Measurements using individual nanotubes with determined chirality allow quantitative analysis, and chirality dependence of the Stark redshifts shows reasonable agreement with theoretical calculations. As the emission energy in nanotubes are tunable by electric fields, one of the possible ap-

plications is optical switching by integrating nanotube FETs into one-dimensional photonic crystal nanocavities [150].

Finally, we have demonstrated trion emission from electrostatically doped clean nanotubes despite the theoretical expectation that trion formation is difficult due to low exciton-carrier scattering rates. By measuring hundred individual SWCNTs, we successfully extract trion binding energies in suspended nanotubes, which is significantly larger than those of surfactant-wrapped nanotubes because of reduced screening in suspended tubes. Since trions have nonzero charge and are spin-1/2 system, they are promising for applications in nanoscale spintronics devices that utilize nanotubes.

In this dissertation, we have elucidated these electric field effects on excitons in SWCNTs, and we would like to emphasize the importance of measurements using individual chirality-assigned nanotubes. This is because there exist not only band structure dependence on chirality but also inhomogeneous broadening in single-chirality nanotube ensembles. In practice, characterization for each nanotube is timeconsuming, but construction of the automated optical setup allows efficient data collection. As a result, we are able to quantitatively characterize electric field effects on excitons in nanotubes, and we hope that our results will lead to carbon-nanotube-based nanoscale optoelectronic devices.

Appendix A

Raman spectroscopy

Catalyst conditions for carbon nanotube growth as explained in Sec. 2.2 are optimized using Raman spectroscopy. We prepare four samples, which are (i) a SiO₂/Si substrate as a reference sample, (ii) a SiO₂/Si with Co/silica catalyst, (iii) a SiO₂/Si with Fe-thin film catalyst, and (iv) a SiO₂/Si with Fe/Pt/Ti layer. We note that all of the samples are not patterned by lithography, and each catalyst is spread on the substrates except for the reference sample. After catalyst deposition on each sample, the samples are heated in air for 5 min at 400°C, and ethanol CVD is performed at 800°C for 1 min.

Figure A.1 shows Raman spectra of the four samples, and we observe clear RBM¹ (150-300 cm⁻¹) and G band (~1600 cm⁻¹) peaks [151] for sample (ii) and (iii), suggesting that carbon nanotubes grow well. However, sample (i) and (iv) do not show these peaks, and therefore the Fe/Pt layer does not act as catalyst for nanotube growth. This may be caused by alloying between Fe and Pt during heating process in CVD.

In addition, we find that the (iii) Fe catalyst sample shows many RBM peaks compared to the (ii) Co/silica sample [Fig. A.1(b)]. This result indicates that nanotube diameter distribution in the sample (iii) is wider than that in (ii) since nanotube diameters are estimated from the equation which is given by $d = 248/w$, where d (nm) and w (cm⁻¹) are a nanotube diameter and a Raman shift of RBM peaks, respectively.

¹Radial breathing mode

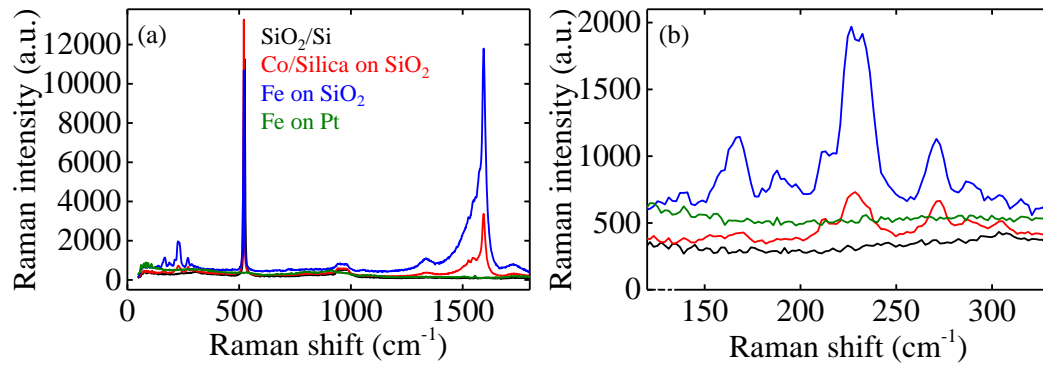


Figure A.1: Raman spectra taken with excitation wavelength of 532 nm and excitation power of 10 mW. We use an inVia Raman microscope (Renishaw), and the magnification of an objective lens is 5. Peaks around 500 cm^{-1} and 950 cm^{-1} are induced by Si, and peaks at 1300 cm^{-1} corresponds to a defect induced mode from carbon.

Appendix B

Heat conduction equation

We show the detailed calculation which is explained in Sec. 3.3.3.

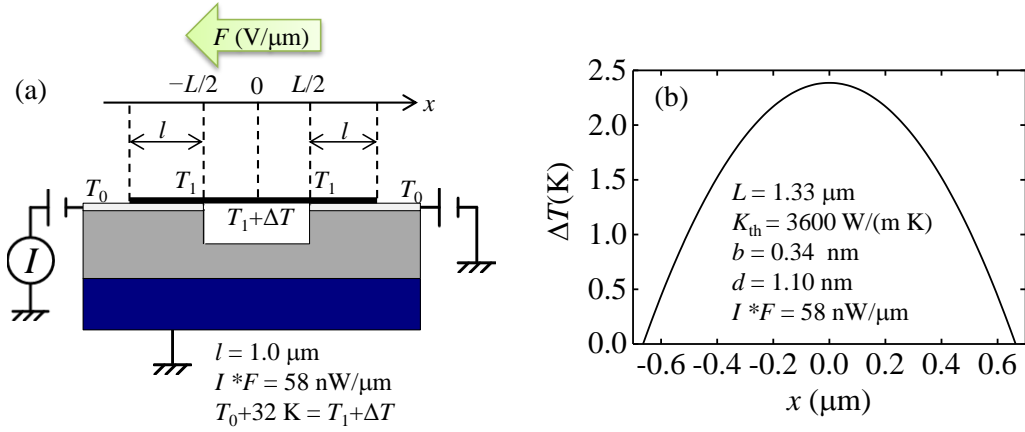


Figure B.1: (a) A calculation model for temperature. (b) Temperature increase ΔT as a function of nanotube position x .

A calculation model is described in Fig. B.1(a), and we assume that temperatures at Pt electrodes and a nanotube on edges of a trench are fixed at T_0 and T_1 , respectively. When Joule heating IF is $58 \text{ nW}/\mu\text{m}$, temperature at the center of the nanotube is $T_0 + 32 \text{ K}$ which is estimated from linewidth broadening of PL. In this case, the heat conduction equation is given by

$$A\kappa_{th} \frac{d^2}{dx^2} T(x) + IF = 0 \quad (\text{B.1})$$

$$T\left(x = \pm \frac{L}{2}\right) = T_1 \quad (\text{Boundary conditions}), \quad (\text{B.2})$$

where x is a nanotube axial coordinate, $L = 1.33 \mu\text{m}$ is the tube length, $\kappa_{th} =$

3600 W/(m K) is a thermal conductivity,¹ and $A = \pi db$ is the cross sectional area ($b = 0.34$ nm is the tube wall thickness, and $d = 1.10$ nm is the tube diameter) [134]. By solving the heat conduction equation, we obtain

$$T(x) = -\frac{1}{2} \frac{IF}{A\kappa_{th}} x^2 + \frac{1}{2} \frac{IF}{A\kappa_{th}} \frac{L^2}{4} + T_1, \quad (\text{B.3})$$

and simulate the heating profile of the nanotube [Fig. B.1(b)], where ΔT is the temperature increase from the tube on the edges of trenches. We find that $\Delta T(x = 0) = 2.4\text{K}$, and most of the temperature increase of the tube is caused at the nanotube contacts. Thus, we calculate a thermal contact resistance κ_c as follows

$$\kappa_c = \frac{(T_1 - T_0)l}{IF} \sim 490 \text{ K m/W}, \quad (\text{B.4})$$

where the contact length l is 1 μm .

¹Indeed, there exists temperature dependence of the thermal conductivity [152], but the change in the thermal conductivity at room temperature is limited when the tube temperature increase is $\sim 32\text{K}$. We therefore assume that the thermal conductivity is a fixed value.

References

- [1] S. Iijima,, T. Ichihashi, *Nature* **363**, 603 (1993).
- [2] R. Saito, G. Dresselhaus, M. S. Dresselhaus, *Physical Properties of Carbon Nanotubes* (Imperial College Press, London, 1998).
- [3] S. Reich, C. Thomsen, J. Maultzsch, *Carbon Nanotubes -Basic Concepts and Physical Properties-* (WILEY-VCH, 2003).
- [4] M. Yoshida, Construction of an optically-detected magnetic resonance microscope, Master's thesis, The Univ. of Tokyo (2012).
- [5] N. Hamada, S. Sawada, A. Oshiyama, *Phys. Rev. Lett.* **68**, 1579 (1992).
- [6] R. Saito, M. Fujita, G. Dresselhaus, M. S. Dresselhaus, *Appl. Phys. Lett.* **60**, 2204 (1992).
- [7] H. Ajiki, T. Ando, *Japanese Journal of Applied Physics* **34**, 107 (1995).
- [8] C. D. Spataru, S. Ismail-Beigi, L. X. Benedict, S. G. Louie, *Appl. Phys. A* **78**, 1129 (2004).
- [9] J. Lefebvre, P. Finnie, *Phys. Rev. Lett.* **98**, 167406 (2007).
- [10] J. Lefebvre, J. M. Fraser, P. Finnie, Y. Homma, *Phys. Rev. B* **69**, 075403 (2004).
- [11] M. J. O'Connell, S. M. Bachilo, C. B. Huffman, V. C. Moore, M. S. Strano, E. H. Haroz, K. L. Rialon, P. J. Boul, W. H. Noon, C. Kittrell, J. Ma, R. H. Hauge, R. B. Weisman, R. E. Smalley, *Science* **297**, 593 (2002).

- [12] L. Lüer, S. Hoseinkhani, D. Polli, J. Crochet, T. Hertel, G. Lanzani, *Nat. Phys.* **5**, 54 (2009).
- [13] T. Ando, *J. Phys. Soc. Jpn.* **66**, 1066 (1997).
- [14] F. Wang, G. Dukovic, L. E. Brus, T. F. Heinz, *Science* **308**, 838 (2005).
- [15] J. Maultzsch, R. Pomraenke, S. Reich, E. Chang, D. Prezzi, A. Ruini, E. Molinari, M. S. Strano, C. Thomsen, C. Lienau, *Phys. Rev. B* **72**, 241402(R) (2005).
- [16] J. Lefebvre, P. Finnie, *Nano Lett.* **8**, 1890 (2008).
- [17] T. Ando, *J. Phys. Soc. Jpn.* **75**, 024707 (2006).
- [18] H. Ajiki, T. Ando, *Physica B* **201**, 349 (1994).
- [19] S. Zaric, G. N. Ostojic, J. Kono, J. Shaver, V. C. Moore, M. S. Strano, R. H. Hauge, R. E. Smalley, X. Wei, *Science* **304**, 1129 (2004).
- [20] S. Zaric, G. N. Ostojic, J. Shaver, J. Kono, O. Portugall, P. H. Frings, G. L. J. A. Rikken, M. Furis, S. A. Crooker, X. Wei, V. C. Moore, R. H. Hauge, R. E. Smalley, *Phys. Rev. Lett.* **96**, 016406 (2006).
- [21] R. Matsunaga, K. Matsuda, Y. Kanemitsu, *Phys. Rev. Lett.* **101**, 147404 (2008).
- [22] I. B. Mortimer, R. J. Nicholas, *Phys. Rev. Lett.* **98**, 027404 (2007).
- [23] Y. Murakami, B. Lu, S. Kazaoui, N. Minami, T. Okubo, S. Maruyama, *Phys. Rev. B* **79**, 195407 (2009).
- [24] O. N. Torrens, M. Zheng, J. M. Kikkawa, *Phys. Rev. Lett.* **101**, 157401 (2008).
- [25] P. M. Vora, X. Tu, E. J. Mele, M. Zheng, J. M. Kikkawa, *Phys. Rev. B* **81**, 155123 (2010).

- [26] A. D. Mohite, T. S. Santos, J. S. Moodera, B. W. Alphenaar, *Nat. Nanotech.* **4**, 425 (2009).
- [27] R. Matsunaga, K. Matsuda, Y. Kanemitsu, *Phys. Rev. B* **81**, 033401 (2010).
- [28] K. Nagatsu, S. Chiashi, S. Konabe, Y. Homma, *Phys. Rev. Lett.* **105**, 157403 (2010).
- [29] T. F. Rønnow, T. G. Pedersen, H. D. Cornean, *Phys. Rev. B* **81**, 205446 (2010).
- [30] M. A. Lampert, *Phys. Rev. Lett.* **1**, 450 (1958).
- [31] C. Galland, A. Imamoğlu, *Phys. Rev. Lett.* **101**, 157404 (2008).
- [32] R. Matsunaga, K. Matsuda, Y. Kanemitsu, *Phys. Rev. Lett.* **106**, 037404 (2011).
- [33] S. M. Santos, B. Yuma, S. Berciaud, J. Shaver, M. Gallart, P. Gilliot, L. Cagnet, B. Lounis, *Phys. Rev. Lett.* **107**, 187401 (2011).
- [34] K. Watanabe, K. Asano, *Phys. Rev. B* **85**, 035416 (2012).
- [35] I. V. Bondarev, *Phys. Rev. B* **90**, 245430 (2014).
- [36] T. Deilmann, M. Drüppel, M. Rohlfing, *Phys. Rev. Lett.* **116**, 196804 (2016).
- [37] K. Kheng, R. T. Cox, M. Y. d' Aubigné, F. Bassani, K. Saminadayar, S. Tatarenko, *Phys. Rev. Lett.* **71**, 1752 (1993).
- [38] K. F. Mak, K. He, C. Lee, G. H. Lee, J. Hone, T. F. Heinz, J. Shan, *Nat. Mater.* **12**, 207 (2013).
- [39] J. Kong, H. T. Soh, A. M. Cassell, C. F. Quate, H. Dai, *Nature* **395**, 878 (1998).
- [40] S. J. Tans, M. H. Devoret, H. Dai, A. Thess, R. E. Smalley, L. J. Geerligs, C. Dekker, *Nature* **386**, 474 (1997).

- [41] S. J. Tans, A. R. M. Verschueren, C. Dekker, *Nature* **393**, 49 (1998).
- [42] P. Avouris, M. Freitag, V. Perebeinos, *Nat. Photon.* **2**, 341 (2008).
- [43] S. M. Bachilo, M. S. Strano, C. Kittrell, R. H. Hauge, R. E. Smalley, R. B. Weisman, *Science* **298**, 2361 (2002).
- [44] R. B. Capaz, C. D. Spataru, S. Ismail-Beigi, S. G. Louie, *Phys. Rev. B* **74**, 121401(R) (2006).
- [45] J. Jiang, R. Saito, G. G. Samsonidze, A. Jorio, S. G. Chou, G. Dresselhaus, M. S. Dresselhaus, *Phys. Rev. B* **75**, 235408 (2007).
- [46] V. C. Moore, M. S. Strano, E. H. Haroz, R. H. Hauge, R. E. Smalley, J. Schmidt, Y. Talmon, *Nano Lett.* **3**, 1379 (2003).
- [47] Y. Ohno, S. Iwasaki, Y. Murakami, S. Kishimoto, S. Maruyama, T. Mizutani, *Phys. Rev. B* **73**, 235427 (2006).
- [48] Y. Ohno, S. Iwasaki, Y. Murakami, S. Kishimoto, S. Maruyama, T. Mizutani, *Phys. Status Solidi B* **244**, 4002 (2007).
- [49] S. Chiashi, S. Watanabe, T. Hanashima, Y. Homma, *Nano Lett.* **8**, 3097 (2008).
- [50] J. A. Misewich, R. Martel, P. Avouris, J. C. Tsang, S. Heinze, J. Tersoff, *Science* **300**, 783 (2003).
- [51] J. Chen, V. Perebeinos, M. Freitag, J. Tsang, Q. Fu, J. Liu, P. Avouris, *Science* **310**, 1171 (2005).
- [52] D. Mann, Y. K. Kato, A. Kinkhabwala, E. Pop, J. Cao, X. Wang, L. Zhang, Q. Wang, J. Guo, H. Dai, *Nat. Nanotech.* **2**, 33 (2007).
- [53] T. Mueller, M. Kinoshita, M. Steiner, V. Perebeinos, A. A. Bol, D. B. Farmer, P. Avouris, *Nat. Nanotech.* **5**, 27 (2010).
- [54] T. Mori, Y. Yamauchi, S. Honda, H. Maki, *Nano Lett.* **14**, 3277 (2014).

- [55] Y. Miyauchi, Z. Zhang, M. Takekoshi, Y. Tomio, H. Suzuura, V. Perebeinos, V. V. Deshpande, C. Lu, S. Berciaud, P. Kim, J. Hone, T. F. Heinz, *Phys. Rev. B* **92**, 205407 (2015).
- [56] A. W. Bushmaker, V. V. Deshpande, S. Hsieh, M. W. Bockrath, S. B. Cronin, *Phys. Rev. Lett.* **103**, 067401 (2009).
- [57] M. Steiner, M. Freitag, V. Perebeinos, A. Naumov, J. P. Small, A. A. Bol, P. Avouris, *Nano Lett.* **9**, 3477 (2009).
- [58] L. Nienhaus, S. Wiegold, D. Nguyen, J. W. Lyding, G. E. Scott, M. Gruebele, *ACS Nano* **9**, 10563 (2015).
- [59] V. Perebeinos, P. Avouris, *Nano Lett.* **7**, 609 (2007).
- [60] H. Zhao, S. Mazumdar, *Phys. Rev. Lett.* **98**, 166805 (2007).
- [61] M. L. Trolle, T. G. Pedersen, *Phys. Rev. B* **92**, 085431 (2015).
- [62] C. D. Spataru, F. Léonard, *Phys. Rev. Lett.* **104**, 177402 (2010).
- [63] T. Takenobu, Y. Murayama, Y. Iwasa, *Appl. Phys. Lett.* **89**, (2006).
- [64] M.-H. Ham, B.-S. Kong, W.-J. Kim, H.-T. Jung, M. S. Strano, *Phys. Rev. Lett.* **102**, 047402 (2009).
- [65] T. Ogawa, S. Watanabe, N. Minami, R. Shimano, *Appl. Phys. Lett.* **97**, (2010).
- [66] H. Kishida, Y. Nagasawa, S. Imamura, A. Nakamura, *Phys. Rev. Lett.* **100**, 097401 (2008).
- [67] M. Freitag, Y. Martin, J. A. Misewich, R. Martel, P. Avouris, *Nano Lett.* **3**, 1067 (2003).
- [68] Y. L. Kim, H. Y. Jung, S. Park, B. Li, F. Liu, J. Hao, Y.-K. Kwon, Y. J. Jung, S. Kar, *Nat. Photon.* **8**, 239 (2014).
- [69] J. U. Lee, *Phys. Rev. B* **75**, 075409 (2007).

- [70] N. M. Gabor, Z. Zhong, K. Bosnick, J. Park, P. L. McEuen, *Science* **325**, 1367 (2009).
- [71] T. Uda, M. Yoshida, A. Ishii, Y. K. Kato, *Nano Lett.* **16**, 2278 (2016).
- [72] A. Malapanis, V. Perebeinos, D. P. Sinha, E. Comfort, J. U. Lee, *Nano Lett.* **13**, 3531 (2013).
- [73] S. Kazaoui, S. Cook, N. Izard, Y. Murakami, S. Maruyama, N. Minami, *J. Phys. Chem. C* **118**, 18059 (2014).
- [74] L. Prechtel, L. Song, S. Manus, D. Schuh, W. Wegscheider, A. W. Holleitner, *Nano Lett.* **11**, 269 (2011).
- [75] A. D. Mohite, P. Gopinath, H. M. Shah, B. W. Alphenaar, *Nano Lett.* **8**, 142 (2008).
- [76] M. Barkelid, V. Zwiller, *Nat. Photon.* **8**, 47 (2014).
- [77] T. DeBorde, L. Aspirtarte, T. Sharf, J. W. Kevek, E. D. Minot, *ACS Nano* **8**, 216 (2014).
- [78] G. Buchs, S. Bagiante, G. Steele, *Nat. Commun.* **5**, 4987 (2014).
- [79] S.-W. Chang, J. Theiss, J. Hazra, M. Aykol, R. Kapadia, S. B. Cronin, *Appl. Phys. Lett.* **107**, 053107 (2015).
- [80] S.-W. Chang, J. Hazra, M. Amer, R. Kapadia, S. B. Cronin, *ACS Nano* **9**, 11551 (2015).
- [81] J. U. Lee, *Appl. Phys. Lett.* **87**, 073101 (2005).
- [82] K. Balasubramanian, M. Burghard, K. Kern, M. Scolari, A. Mews, *Nano Lett.* **5**, 507 (2005).
- [83] A. W. Tsen, L. A. K. Donev, H. Kurt, L. H. Herman, J. Park, *Nat. Nanotech.* **4**, 108 (2008).
- [84] Y. Ohno, S. Kishimoto, T. Mizutani, *Nanotechnology* **17**, 549 (2006).

- [85] A. V. Naumov, S. M. Bachilo, D. A. Tsyboulski, R. B. Weisman, *Nano Lett.* **8**, 1527 (2008).
- [86] M. Freitag, M. Steiner, A. Naumov, J. P. Small, A. A. Bol, V. Perebeinos, P. Avouris, *ACS Nano* **3**, 3744 (2009).
- [87] S. Yasukochi, T. Murai, S. Moritsubo, T. Shimada, S. Chiashi, S. Maruyama, Y. K. Kato, *Phys. Rev. B* **84**, 121409(R) (2011).
- [88] M. Jiang, Y. Kumamoto, A. Ishii, M. Yoshida, T. Shimada, Y. K. Kato, *Nat. Commun.* **6**, 6335 (2015).
- [89] K. Matsuda, Y. Miyauchi, T. Sakashita, Y. Kanemitsu, *Phys. Rev. B* **81**, 033409 (2010).
- [90] V. Perebeinos, P. Avouris, *Phys. Rev. Lett.* **101**, 057401 (2008).
- [91] H. Hartleb, F. Späth, T. Hertel, *ACS Nano* **9**, 10461 (2015).
- [92] J. S. Park, Y. Hirana, S. Mouri, Y. Miyauchi, N. Nakashima, K. Matsuda, *J. Am. Chem. Soc.* **134**, 14461 (2012).
- [93] H. Liu, D. Nishide, T. Tanaka, H. Kataura, *Nat. Commun.* **2**, 309 (2011).
- [94] F. Yang, X. Wang, D. Zhang, J. Yang, D. Luo, Z. Xu, J. Wei, J.-Q. Wang, Z. Xu, F. Peng, et al., *Nature* **510**, 522 (2014).
- [95] J. R. Sanchez-Valencia, T. Dienel, O. Gröning, I. Shorubalko, A. Mueller, M. Jansen, K. Amsharov, P. Ruffieux, R. Fasel, *Nature* **512**, 61 (2014).
- [96] A. Hartschuh, H. N. Pedrosa, L. Novotny, T. D. Krauss, *Science* **301**, 1354 (2003).
- [97] T. Odom, J. Huang, P. Kim, C. Lieber, *Nature* **391**, 62 (1998).
- [98] M. Gao, J. M. Zuo, R. D. Twisten, I. Petrov, L. A. Nagahara, R. Zhang, *Appl. Phys. Lett.* **82**, 2703 (2003).
- [99] A. Ishii, M. Yoshida, Y. K. Kato, *Phys. Rev. B* **91**, 125427 (2015).

- [100] T. DeBorde, L. Aspirtarte, T. Sharf, J. W. Kevek, E. D. Minot, *J. Phys. Chem. C* **118**, 9946 (2014s).
- [101] Y. Kumamoto, M. Yoshida, A. Ishii, A. Yokoyama, T. Shimada, Y. K. Kato, *Phys. Rev. Lett.* **112**, 117401 (2014).
- [102] M. Yoshida, Y. Kumamoto, A. Ishii, A. Yokoyama, Y. K. Kato, *Appl. Phys. Lett.* **105**, 161104 (2014).
- [103] M. Yoshida, A. Popert, Y. K. Kato, *Phys. Rev. B* **93**, 041402(R) (2016).
- [104] Y. Kumamoto, Photoluminescence and photocurrent measurements of individual air-suspended carbon nanotubes under longitudinal electric fields, Master's thesis, The Univ. of Tokyo (2013).
- [105] T. Inoue, D. Hasegawa, S. Badar, S. Aikawa, S. Chiashi, S. Maruyama, *J. Phys. Chem. C* **117**, 11804 (2013).
- [106] S. Maruyama, R. Kojima, Y. Miyauchi, S. Chiashi, M. Kohno, *Chem. Phys. Lett.* **360**, 229 (2002).
- [107] S. Imamura, R. Watahiki, R. Miura, T. Shimada, Y. K. Kato, *Appl. Phys. Lett.* **102**, 161102 (2013).
- [108] N. Higashide, Electroluminescence and photoluminescence from individual air-suspended carbon nanotubes within split-gate structures, Master's thesis, The Univ. of Tokyo (2016).
- [109] S. Moritsubo, T. Murai, T. Shimada, Y. Murakami, S. Chiashi, S. Maruyama, Y. K. Kato, *Phys. Rev. Lett.* **104**, 247402 (2010).
- [110] M. Freitag, J. C. Tsang, A. Bol, P. Avouris, D. Yuan, J. Liu, *Appl. Phys. Lett.* **91**, 031101 (2007).
- [111] Y. H. Ahn, A. W. Tsen, B. Kim, Y. W. Park, J. Park, *Nano Lett.* **7**, 3320 (2007).

- [112] N. Rauhut, M. Engel, M. Steiner, R. Krupke, P. Avouris, A. Hartschuh, *ACS Nano* **6**, 6416 (2012).
- [113] T. Ogawa, T. Takagahara, *Phys. Rev. B* **44**, 8138 (1991).
- [114] F. Schöppler, C. Mann, T. C. Hain, F. M. Neubauer, G. Privitera, F. Bonaccorso, D. Chu, A. C. Ferrari, T. Hertel, *J. Phys. Chem. C* **115**, 14682 (2011).
- [115] J. U. Lee, P. J. Codella, M. Pietrzykowski, *Appl. Phys. Lett.* **90**, 053103 (2007).
- [116] M. Barkelid, G. A. Steele, V. Zwiller, *Nano Lett.* **12**, 5649 (2012).
- [117] J. U. Lee, *Phys. Rev. B* **75**, 075409 (2007).
- [118] K. Matsuda, T. Inoue, Y. Murakami, S. Maruyama, Y. Kanemitsu, *Phys. Rev. B* **77**, 033406 (2008).
- [119] Y. Murakami, J. Kono, *Phys. Rev. B* **80**, 035432 (2009).
- [120] Y.-F. Xiao, T. Q. Nhan, M. W. B. Wilson, J. M. Fraser, *Phys. Rev. Lett.* **104**, 017401 (2010).
- [121] V. Perebeinos, J. Tersoff, P. Avouris, *Phys. Rev. Lett.* **92**, 257402 (2004).
- [122] T. Hertel, V. Perebeinos, J. Crochet, K. Arnold, M. Kappes, P. Avouris, *Nano Lett.* **8**, 87 (2008).
- [123] L. Oudjedi, A. N. G. Parra-Vasquez, A. G. Godin, L. Cognet, B. Lounis, *J. Phys. Chem. Lett.* **4**, 1460 (2013).
- [124] D. Y. Joh, J. Kinder, L. H. Herman, S.-Y. Ju, M. A. Segal, J. N. Johnson, G. K.-L. Chan, J. Park, *Nat. Nanotech.* **6**, 51 (2011).
- [125] J. J. Sakurai, J. Napolitano, *Modern Quantum Mechanics* (Addison-Wesley, San Francisco, edn. 2, 2011).

- [126] D. M. Harrah, J. R. Schneck, A. A. Green, M. C. Hersam, L. D. Ziegler, A. K. Swan, *ACS Nano* **5**, 9898 (2011).
- [127] G. Soavi, F. Scotognella, D. Brida, T. Hefner, F. Spath, M. R. Antognazza, T. Hertel, G. Lanzani, G. Cerullo, *J. Phys. Chem. C* **117**, 10849 (2013).
- [128] C. Georgi, A. A. Green, M. C. Hersam, A. Hartschuh, *ACS Nano* **4**, 5914 (2010).
- [129] K. Matsuda, T. Inoue, Y. Murakami, S. Maruyama, Y. Kanemitsu, *Phys. Rev. B* **77**, 193405 (2008).
- [130] A. Högele, C. Galland, M. Winger, A. Imamoğlu, *Phys. Rev. Lett.* **100**, 217401 (2008).
- [131] A. D. Franklin, Z. Chen, *Nat. Nanotech.* **5**, 858 (2010).
- [132] J. Lefebvre, P. Finnie, Y. Homma, *Phys. Rev. B* **70**, 045419 (2004).
- [133] K. Yoshikawa, R. Matsunaga, K. Matsuda, Y. Kanemitsu, *Appl. Phys. Lett.* **94**, (2009).
- [134] E. Pop, D. Mann, J. Cao, Q. Wang, K. Goodson, H. Dai, *Phys. Rev. Lett.* **95**, 155505 (2005).
- [135] M. T. Pettes, L. Shi, *Adv. Funct. Mater.* **19**, 3918 (2009).
- [136] G. Dukovic, F. Wang, D. Song, M. Y. Sfeir, T. F. Heinz, L. E. Brus, *Nano Lett.* **5**, 2314 (2005).
- [137] J. S. Ross, S. Wu, H. Yu, N. J. Ghimire, A. M. Jones, G. Aivazian, J. Yan, D. G. Mandrus, D. Xiao, W. Yao, X. Xu, *Nat. Commun.* **4**, 1474 (2013).
- [138] S. Mouri, Y. Miyauchi, M. Iwamura, K. Matsuda, *Phys. Rev. B* **87**, 045408 (2013).
- [139] N. Akizuki, M. Iwamura, S. Mouri, Y. Miyauchi, T. Kawasaki, H. Watanabe, T. Suemoto, K. Watanabe, K. Asano, K. Matsuda, *Phys. Rev. B* **89**, 195432 (2014).

- [140] F. Jakubka, S. B. Grimm, Y. Zakharko, F. Gannott, J. Zaumseil, *ACS Nano* **8**, 8477 (2014).
- [141] T. Koyama, S. Shimizu, Y. Miyata, H. Shinohara, A. Nakamura, *Phys. Rev. B* **87**, 165430 (2013).
- [142] T. Nishihara, Y. Yamada, M. Okano, Y. Kanemitsu, *Appl. Phys. Lett.* **103**, 023101 (2013).
- [143] B. Yuma, S. Berciaud, J. Besbas, J. Shaver, S. Santos, S. Ghosh, R. B. Weisman, L. Cognet, M. Gallart, M. Ziegler, B. Hönerlage, B. Lounis, P. Gilliot, *Phys. Rev. B* **87**, 205412 (2013).
- [144] S. Konabe, K. Matsuda, S. Okada, *Phys. Rev. Lett.* **109**, 187403 (2012).
- [145] R. Watahiki, T. Shimada, P. Zhao, S. Chiashi, S. Iwamoto, Y. Arakawa, S. Maruyama, Y. K. Kato, *Appl. Phys. Lett.* **101**, 141124 (2012).
- [146] A. Yokoyama, M. Yoshida, A. Ishii, Y. K. Kato, *Phys. Rev. X* **4**, 011005 (2014).
- [147] A. Ishii, Exciton diffusion and related exciton decay processes in air-suspended single-walled carbon nanotubes studied by photoluminescence spectroscopy, Master's thesis, The Univ. of Tokyo (2014).
- [148] W. Kim, A. Javey, O. Vermesh, Q. Wang, Y. Li, H. Dai, *Nano Lett.* **3**, 193 (2003).
- [149] S. Mouri, K. Matsuda, *J. Appl. Phys.* **111**, 094309 (2012).
- [150] F. Pyatkov, V. Fütterling, S. Khasminskaya, B. S. Flavel, F. Henrich, M. M. Kappes, R. Krupke, W. H. P. Pernice, *Nat. Photon.* **10**, 420 (2016).
- [151] R. Saito, M. Hofmann, G. Dresselhaus, A. Jorio, M. S. Dresselhaus, *Advances in Physics* **60**, 413 (2011).
- [152] E. Pop, D. Mann, Q. Wang, K. Goodson, H. Dai, *Nano Lett.* **6**, 96 (2006).

List of publications and presentations

Publications

- [1] T. Uda, M. Yoshida, A. Ishii, and Y. K. Kato, “Electric-Field Induced Activation of Dark Excitonic States in Carbon nanotubes”, *Nano Lett.* **16**, 2278 (2016).
- [2] M. Yoshida, A. Popert, and Y. K. Kato, “Gate-voltage induced trions in suspended carbon nanotubes”, *Phys. Rev. B* **93**, 041402(R) (2016) (Editors’ suggestion).
- [3] A. Ishii, M. Yoshida, and Y. K. Kato, “Exciton diffusion, end quenching, and exciton-exciton annihilation in individual air-suspended carbon nanotubes”, *Phys. Rev. B* **91**, 125427 (2015).
- [4] M. Jiang, Y. Kumamoto, A. Ishii, M. Yoshida, T. Shimada, and Y. K. Kato, “Gate-controlled generation of optical pulse trains using individual carbon nanotubes”, *Nat. Commun.* **6**, 6335 (2015).
- [5] M. Yoshida, Y. Kumamoto, A. Ishii, A. Yokoyama, and Y. K. Kato, “Stark effect of excitons in individual air-suspended carbon nanotubes”, *Appl. Phys. Lett.* **105**, 161104 (2014).
- [6] Y. Kumamoto, M. Yoshida, A. Ishii, A. Yokoyama, T. Shimada, and Y. K. Kato, “Spontaneous exciton dissociation in carbon nanotubes”, *Phys. Rev. Lett.* **112**, 117401 (2014).

- [7] A. Yokoyama, M. Yoshida, A. Ishii, and Y. K. Kato, “Giant circular dichroism in individual carbon nanotubes induced by extrinsic chirality”, *Phys. Rev. X* **4**, 011005 (2014).

Oral presentations (International conferences)

- [8] M. Yoshida, A. Popert, Y. K. Kato, “Gate-voltage induced trions in suspended carbon nanotubes”, March Meeting of the American Physical Society, Baltimore, Maryland, USA (March 15, 2016).
- [9] M. Yoshida, Y. Kumamoto, A. Ishii, A. Yokoyama, Y. K. Kato, “Stark effect of excitons in individual air-suspended carbon nanotubes”, March Meeting of the American Physical Society, San Antonio, Texas (March, 2015).
- [10] M. Yoshida, Y. Kumamoto, A. Ishii, A. Yokoyama, T. Shimada, and Y. K. Kato, “Spontaneous Exciton Dissociation and Stark Effect in Carbon Nanotubes”, NT14 Satellite Symposium, Los Angeles, California (June, 2014).
- [11] M. Yoshida, Y. Kumamoto, A. Ishii, A. Yokoyama, T. Shimada, and Y. K. Kato, “Spontaneous exciton dissociation in carbon nanotubes”, March Meeting of the American Physical Society, Denver, Colorado (March, 2014).

Poster presentations (International conferences)

- [12] M. Yoshida, A. Popert, Y. K. Kato, “Gate-voltage induced trions in individual air-suspended carbon nanotubes”, The Sixteenth International Conference on the Science and Application of Nanotubes (NT15), Nagoya, Japan (June 30, 2015).
- [13] M. Yoshida, A. Popert, Y. K. Kato, “Gate-voltage induced trions in individual air-suspended carbon nanotubes”, Ninth International Workshop on Metrology, Standardization and Industrial Quality of Nanotubes (MSIN15), Nagoya, Japan (June 28, 2015).

- [14] M. Yoshida, A. Popert, Y. K. Kato, “Gate-voltage induced trions in individual air-suspended carbon nanotubes”, 6th Workshop on Nanotube Optics and Nanospectroscopy (WONTON15), Kloster Banz, Germany (June 3, 2015).
- [15] M. Yoshida, Y. Kumamoto, A. Ishii, A. Yokoyama, T. Shimada, and Y. K. Kato, “Spontaneous Exciton Dissociation and Stark Effect in Carbon Nanotubes”, NT14, Los Angeles, California (June, 2014).
- [16] M. Yoshida, A. Yokoyama, A. Ishii, and Y. K. Kato, “Giant circular dichroism in individual carbon nanotubes”, 7th International School and Conference on Spintronics and Quantum Information Technology, Chicago, Illinois (July, 2013).
- [17] M. Yoshida, Y. Kumamoto, A. Ishii, A. Yokoyama, T. Shimada, and Y. K. Kato, “Spontaneous exciton dissociation in carbon nanotubes”, FIRST International Symposium on Topological Quantum Technology, Tokyo, Japan (January, 2014).
- [18] M. Yoshida, A. Yokoyama, S. Yasukochi, and Y. K. Kato, “Construction of an optically-detected magnetic resonance system for investigating spins in single-walled carbon nanotubes”, 6th International School and Conference on Spintronics and Quantum Information Technology, Shimane, Japan (August, 2011).
- [19] M. Yoshida, A. Yokoyama, S. Yasukochi, and Y. K. Kato, “Construction of an optically-detected magnetic resonance system for investigating spins in single-walled carbon nanotubes”, 5th International Workshop on Spin Currents, Miyagi, Japan (July, 2011).

Oral presentations (Domestic conferences)

- [20] M. Yoshida, A. Popert, Y. K. Kato, “Gate-voltage induced trions in suspended carbon nanotubes”, The 50th Fullerenes-Nanotubes-Graphene General Symposium, Tokyo (February 22, 2016).

- [21] M. Yoshida, Y. Kumamoto, A. Ishii, A. Yokoyama, and Y. K. Kato, “Stark effect of excitons in individual air-suspended carbon nanotubes”, The 48th Fullerenes-Nanotubes-Graphene General Symposium, Tokyo (February, 2015).
- [22] M. Yoshida, Y. Kumamoto, A. Ishii, A. Yokoyama, T. Shimada, and Y. K. Kato, “Spontaneous Exciton Dissociation and Stark Effect in Carbon Nanotubes”, The 75th Autumn Meeting of the Japan Society of Applied Physics, Hokkaido (September, 2014).
- [23] M. Yoshida, A. Yokoyama, A. Ishii, and Y. K. Kato, “Giant circular dichroism in individual carbon nanotubes”, The 74th Autumn Meeting of the Japan Society of Applied Physics, Kyoto (September, 2013).